

1 Synoptic- to meso-scale atmospheric circulation connects 2 fluvial and coastal gravel conveyors and directional 3 deposition of coastal landforms in the Dead Sea basin

Formatted: English (United States)

4 Haggai Eyal^{1,2}, Moshe Armon^{1,3}, Yehouda Enzel¹, Nadav G. Lensky^{2,1}

5 ¹The Freddy & Nadin Herrmann Institute of Earth Sciences, The Hebrew University of Jerusalem, The Edmond
6 J. Safra Campus, Givat Ram, Jerusalem 91904, Israel

7 ²Geological Survey of Israel, 32 Yesha'yahu Leibowitz, Jerusalem 9371234, Israel

8 ³Institute for Atmospheric and Climate Science, ETH Zurich, 8092 Zürich, Switzerland

9 *Correspondence to:* Haggai Eyal (haggai.eyal@mail.huji.ac.il) and Nadav G. Lensky (nadav1@gsi.gov.il)

10
11 **Abstract.** Streams convey coarse-clastic sediments towards coasts, where interactions with deltaic and coastal
12 processes determine ~~the~~their resultant ~~landscape morphology.~~ ~~Although extracting sedimentology and~~
13 ~~geomorphology.~~ Extracting hydroclimatic signals from ~~landscapes such environments~~ is a desired goal, ~~many and~~
14 ~~therefore,~~ studies ~~commonly~~ rely on interpreting ~~available~~ paleoclimatic ~~proxies and proxy data, but~~ the link
15 ~~between direct linking of~~ depositional/geomorphic processes ~~and with~~ the hydroclimate remains ~~vague~~obscure.
16 This is a consequence of the challenge to link processes that often are studied separately, span across large spatial
17 and temporal scales including synoptic-scale hydroclimatic forcing, stream flows, water body hydrodynamics,
18 fluvial and coastal sediment transport, and sedimentation. Here, we explore this chain of connected processes in
19 the unique setting of the Dead Sea basin, where present-day hydroclimatology is tied closely with geomorphic
20 evolution and sediment transport of streams and coasts that rapidly respond to lake-level fall. We use a five-years-
21 long (2018-2022) rich dataset of (i) high-resolution synoptic-scale circulation patterns, (ii) continuous wind-wave
22 and rain-floods records, and (iii) storm-scale fluvial and coastal sediment transport of ~~varied mass,~~ 'smart' and
23 marked boulders. We show ~~that the significance of~~ Mediterranean cyclones ~~approaching the eastern~~
24 ~~Mediterranean are in~~ the ~~main circulation pattern that can provide sufficient rainfall and winds that concurrently~~
25 ~~activate two perpendicular sediment conveyors:~~ concurrent activation of fluvial (floods) and coastal (wind-waves)-
26 ~~The~~ sediment conveyors. These synoptic-scale patterns drive the westerlies necessary for (i) delivering the
27 moisture across the Judean desert, which is transformed into floods, and at the same time, (ii) the coeval,
28 topographically funneled winds that turn into surface southerlies ($>10 \text{ m s}^{-1}$) ~~are orographically funneled inside,~~
29 along the Dead Sea rift valley, ~~turning into surface.~~ During winter, these meso-scale southerlies ~~They~~ generate
30 10-30 high-amplitude, northward propagating storm waves ~~per winter,~~ with $<4 \text{ m}$ wave ~~height~~heights. Such
31 ~~storm waves~~ transport cobbles for hundreds of meters alongshore, ~~north of~~northward and away from the supplying
32 channel mouths. ~~Towards~~Four to nine times per winter the ~~decay~~rainfall generated by these atmospheric patterns
33 is capable of the storm wave, the high-altitude synoptic westerlies provide moisture to generate 4-9 flash-
34 generating floods that reach the stream mouths, delivering ~~unsorted~~poorly sorted, coarse gravels ~~into the basin.~~
35 This usually occurs during the decay of the associated storm waves. These gravels are dispersed alongshore by
36 waves ~~only~~during subsequent storms. As storm waves ~~dominates~~dominate and are $>$ five times more frequent than

37 flash-floods, coarse-clastic beach berms and fan-deltas are deposited preferentially north of [the delivering](#) channel
38 mouths. This [asymmetric](#) depositional architecture, controlled by [the regional hydroclimatehydroclimatology](#), is
39 identified for both the modern and Late Pleistocene coast and delta environments, implying that the dominance
40 of present-day Mediterranean cyclones has persisted in the region [sincealso during](#) the Late Pleistocene when
41 Lake Lisan occupied the basin.

42 1. Introduction

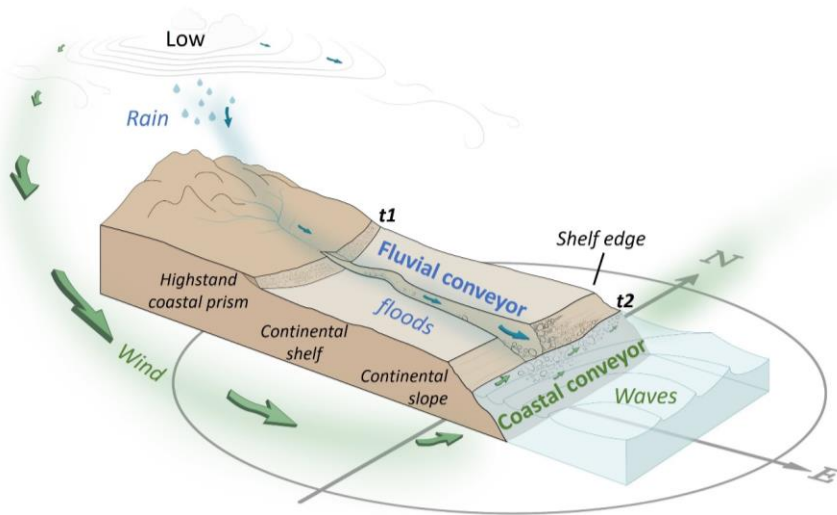
43 Streams and coasts interact and convey coarse sediments. Streams deliver coarse-clastic sediments towards the
44 coast, where the interactions with coastal processes and sediment redistribution in the basin determine deltaic and
45 coastal geomorphology and sedimentology (Ashton et al., 2013; Galloway, 1975; Postma, 1995). While modern
46 [and Late Quaternary](#) deltas and coasts are desired areas for settlements, agriculture, and industry (e.g., Syvitski et
47 al., 2009), ancient deltaic and coastal successions are potential reservoirs of hydrocarbons and water (e.g., Elliot,
48 1986). ~~Globally, such reservoirs are formed also under~~ [In cases of](#) receding water levels, when the continental
49 shelf and/or slope are exposed, ~~triggering evolution of streams in response to base level fall, and such reservoirs~~
50 ~~are formed as~~ coarse ~~sediment-delivery~~ [sediments are delivered](#) from highstand to lowstand deltas ~~and~~
51 ~~subsequently redistributed alongshore~~ (e.g., Blum et al., 2013) (Fig. 1). ~~Despite the importance of understanding~~
52 ~~common controls over these jointly operating coarse-clastic conveyors, they are commonly studied separately.~~

53 Deltaic architecture is defined on the one hand, by the fluvial regime depending on the hinterland characteristics
54 of the watershed, where climate generates flows carrying sediment load into basins. On the other hand, sediment
55 redistribution and deposition are dictated by the ~~basin's~~ shape, size, ~~and bathymetry-of-a-basin~~, and by the
56 hydrodynamics of waves, currents, tides, and the rate of level changes of the water body occupying the basin (see
57 Fig. 1 in Coleman and Prior, 1982; Postma, 1990; Elliot, 1986). ~~This~~ [Nienhuis et al., \(2016\) suggested that channel](#)
58 [orientation of wave-influenced deltas is preserved in the morphology of deltas and has the potential to indicate](#)
59 [past and present fluvial and alongshore sediment transport fluxes. However, commonly the](#) wide range of
60 influencing factors results in diverse types of deltaic depositional configurations (Postma, 1990, 1995), from
61 which it is challenging to decode hydroclimatic and environmental signals, even in modern environments and
62 more so from past sedimentary records (Hansford and Plink-Björklund, 2020). ~~Moreover, despite the importance~~
63 ~~of understanding common controls over fluvial and coastal sediment conveyors, frequently they are studied~~
64 ~~separately.~~

65 In modern *fluvial sediment conveyors*, atmospheric circulation patterns (CPs) and their association with rainfall
66 and floods are extensively studied for specific watersheds and regions (e.g., Bárdossy and Filiz, 2005; Steirou et
67 al., 2017; Merz et al., 2021; Kahana et al., 2002). However, linking the CPs with sediment transport is lacking. A
68 separate body of research deals with flows in channels, their resultant bedload sediment transport (e.g., Reid et
69 al., 1985; Wang et al., 2015; Lekach and Enzel, 2021), channel morphology (e.g., Montgomery and Buffington,
70 1997), and channel mouth deposition (e.g., Bridge, 1993; Wright, 1977; Coleman and Prior, 1982). In modern
71 *coastal conveyors*, ~~along the shores of oceans or lakes~~ [a large body of research deals with global-scale climate](#)
72 [signals and beach change \(e.g., Masselink et al., 2023\).](#) However, only a small number of studies have associated
73 *synoptic-scale* CPs with wave climates ~~along the shores of oceans or lakes~~ (Pringle et al., 2014, 2015; Solari and
74 Alonso, 2017; Graf et al., 2013), few of them ~~also~~ attributed these processes to either longshore transport of sand
75 (e.g., Goodwin et al., 2016) or shoreline erosion (Meadows et al., 1997; Pringle and Stretch, 2021). This small
76 body of research stems from the complex link between synoptic-scale circulation, waves, and their resultant
77 sediment transport; processes occurring over a wide range of spatiotemporal scales (Pringle et al., 2015, 2014,
78 2021; Solari and Alonso, 2017). Therefore, our knowledge regarding the joint fluvial and coastal environments is
79 fragmented, ~~i.e.~~, full linking of the chain of processes/environments, from the synoptic-scale circulation
80 conditions that generate rainstorms-floods, to wind-waves and ~~to~~ sediment transport and deposition in each of the
81 sediment conveyors and their interactions, is missing.

82 The modern Dead Sea (see regional setting in the next Sect.) is a unique environment providing a “natural
83 laboratory” to [potentially](#) study these processes [together](#). It has several advantages: (i) The small to medium-scale
84 watersheds (10^1 - 10^3 kms) surrounding the lake (e.g., Enzel et al., 2008; Zoccatelli et al., 2019) enable ~~to deeply~~
85 ~~studystudying~~ the relative impact of different CPs on water discharge (Enzel et al., 2003; Kahana et al., 2002;
86 Dayan and Morin, 2006) and sediment delivery to the basin (Armon et al., 2018; Ben Dor et al., 2018; Armon et
87 al., 2019). ~~Armon et al., (2018) have linked the rain- and flood-generating CPs and the resulting sediment plumes~~
88 ~~dispersed over the Dead Sea. Linking such sediment dispersion under the lake hydrodynamics is still missing,~~
89 ~~especially for the coarser sediments.~~ (ii) ~~Fluvial~~Rapid fluvial and coastal geomorphic responses ~~occur rapidly in~~
90 ~~response~~ to lake-level fall, ~~enabling~~ [enable](#) a study of real-time geomorphic processes and present-day
91 sedimentary accumulation under forced regression and known environmental forcing with implications to the
92 sedimentary record (e.g., Bartov et al., 2006; Sirota et al., 2021). (iii) ~~Its sedimentary fill is accumulated and well-~~
93 ~~preserved in a terminal basin, thus it is extensively used to reconstruct recent limnology and regional~~
94 ~~paleoclimatology-paleohydrology (e.g., Torfstein et al., 2015, 2013; Huntington, 1911; Neugebauer et al., 2016;~~
95 ~~Kiro et al., 2017; Palchan et al., 2017; Ahlborn et al., 2018; Ben Dor et al., 2018).~~ ~~Despite these advantages,~~
96 ~~interpretations are still mainly inferred based on selected specific proxies and the geomorphic processes that led~~
97 ~~to deposition and their actual link to hydroclimate remains vague.~~
98 ~~Armon et al., (2018) have linked the rain- and flood-generating CPs and the resulted sediment plumes dispersed~~
99 ~~over the Dead Sea. Linking such sediment dispersion under the lake hydrodynamics is still missing, especially of~~
100 ~~coarser sediments.~~ Focusing on gravelly sediments, Eyal et al., (2019) established the recent evolution of an
101 incising stream transporting increasing volumes of gravelly sediment across the Dead Sea shelf, ~~emerging as a~~
102 ~~result of the lake-level fall.~~ Then, ~~from the channel mouth,~~ these coarse sediments are transported ~~and from the~~
103 ~~channel mouth and are~~ sorted alongshore at the nearshore environment under seasonal, storm-wave climates,
104 ~~forming~~ [sorting](#) well-~~sorted~~ [the coarse gravel comprising the](#) coastal landforms (Eyal et al., 2021). However, the
105 spatiotemporal interactions between the stream and coast and the linkage to or the control of the regional and
106 synoptic-~~scale hydroclimatology need elaboration to determine the chain of processes.~~ (iii) ~~Its sedimentary fill is~~
107 ~~well-preserved and accumulated in a terminal basin, thus it is extensively used to reconstruct recent and past~~
108 ~~sequences, limnogeology, earthquakes, and regional paleoclimatology-paleohydrology (e.g., Bookman et al.,~~
109 ~~2004; Bartov et al. 2002, 2006; Torfstein et al., 2015, 2013; Huntington, 1911; Neugebauer et al., 2016; Kiro et~~
110 ~~al., 2017; Palchan et al., 2017; Ahlborn et al., 2018; Ben Dor et al., 2018).~~ ~~scale hydroclimatology needs~~
111 ~~elaboration to determine the chain of processes~~ However, such studies are mainly interpreted based on specific
112 ~~selected proxies and field associations. The geomorphic causative processes leading to deposition and their~~
113 ~~respective links to hydroclimatology remain vague.~~
114 Therefore, we study here present-day climatic controls on coarse fluvial and coastal sediment transport by means
115 of rain, floods, wind, and waves data from the Dead Sea region. We explore ~~the~~ interactions between streams, the
116 coast and the actively forming coarse-clastic sedimentary record (Fig. 1). We search for the specific hydroclimatic
117 events controlling the formation of modern geomorphic/sedimentological record and [for](#) potential insights when
118 interpreting similar past deposits. We use a five-years-long (2018-2022) dataset comprised of (i) high-resolution
119 synoptic-scale circulation conditions, (ii) continuous, wind-wave, and rain-floods records, and (iii) storm-scale
120 fluvial and coastal sediment transport measurements ~~of~~ [by](#) ‘smart’ and marked boulders varying in mass. The
121 manuscript deals with the following questions:

- 122 (1) What ~~is~~are the ~~nature~~characteristics of atmospheric CPs ~~and hydrometeorological conditions activating~~
 123 ~~these during which the~~ fluvial and coastal conveyors? ~~are activated?~~
 124 (2) What are the hydroclimatic thresholds ~~in terms of intensity-duration of the rain, and the magnitude of the~~
 125 ~~floods, winds and waves~~ for transport and deposition of coarse gravel in this currently regressive lake?
 126 ~~Specifically, we focus on intensity-duration of the rainfall, winds, and waves, and the magnitude of the~~
 127 ~~floods.~~
 128 (3) How do rain-producing floods and wind-driven waves interact to generate a coastal geomorphic record
 129 with a specific sedimentary architecture?
 130 (4) What can we learn ~~on past geomorphic records~~ from ~~the~~a modern sedimentary environment
 131 ~~formed/generated~~ by the two ~~sedimentary~~ conveyors ~~on past geomorphic records~~?



132 **Figure 1:** Schematic illustration of the concepts of sediment transport via the stream and coast explored in this study. The
 133 forcing/initiation is at the largest scale; low-pressure atmospheric circulation pattern activates both the fluvial sediment
 134 conveyor by generating rainstorms and floods that transport coarse sediments into a receding basin (blue), and the coastal
 135 sediment conveyor, in which wind-driven waves obliquely attack the beach and generate longshore sediment drift (green).
 136 We discuss the dynamic case during water level lowering. t1 and t2 denote the position of highstand and lowstand
 137 shorelines. In the case of the Dead Sea t1 represents the middle of the 20th century and t2 the 21st century.

138 **2. The Dead Sea Regional settings**

139 The Dead Sea basin ~~is a narrow depression, 150 km long and 15–20 km wide, extending south-north~~ (Fig. 2a)
 140 ~~along~~is an actively subsiding tectonic basin ~~of~~along the Dead Sea transform ~~forming a south-north, 150-km long~~
 141 ~~and 15–20 km wide narrow depression~~ (Garfunkel and Ben-Avraham, 1996). Since the late Miocene, the basin is
 142 occupied by ~~lacustrine water bodies~~lakes, expanding and contracting due to climatically-induced water balance
 143 and the physiography of the basin (e.g., Zak, 1967; Neev and Emery, 1967; Bartov et al., 2002; Manspeizer, 1985).
 144 ~~During/Respectively, during~~ wet and dry climates, the lake ~~level~~levels rose and fell, and its area extended and

145 contracted, ~~respectively~~ (e.g., Bartov et al., 2003, 2006; Bookman et al., [2004](#); 2006; Enzel et al., 2003). The
146 fluvial and coastal geomorphic responses to these fluctuating lake levels have left well-preserved fan-deltas,
147 paleo-shorelines, and mudflats, related to the Late Pleistocene Lake Lisan (Bowman, 1971; Amit and Gerson,
148 1986; [FROSTICK](#)~~Frostick~~ and [REID](#)~~Reid~~, 1989; Abu Ghazleh and Kempe, 2009) and the Holocene Dead Sea
149 (Enzel et al., 2006., and chapters in Enzel and Bar-Yosef, 2017) (Fig. 2a).

150 2.1 Geomorphic evolution of streams and coasts in response to shelf and slope exposure

151 The anthropogenically-induced level decline of the modern Dead Sea, at $>1 \text{ m y}^{-1}$ (Lensky et al., 2005), due to
152 water diversions, results in exposure of landscapes considered as fast-forming analogs to the eustatic emergence
153 of continental shelves and slopes (Dente et al., 2017, 2018; Eyal et al., 2019). The Dead Sea shelf and slope are
154 mainly comprised of [laminated](#) clay silt, ~~laminated~~, lacustrine deposits over which streams (e.g., Dente et al.,
155 2017, 2018, 2021; Ben-Moshe et al., 2008; Bowman et al., 2010; Eyal et al., 2019) and coasts (e.g., Bowman et
156 al., 2000; Bookman et al., 2006; Eyal et al., 2021; Enzel et al., 2022) rapidly evolve and ~~can be~~ studied at the field
157 scale in real-time and at [the](#) storm- to multi-year resolutions. ~~In~~[At](#) the ~~north-western~~[northwestern](#) edge of the lake,
158 at the lower reach of the well-studied ephemeral stream of Nahal (wadi) Og (Fig. 2b-d), hydrological connection
159 with the fast-receding coastline is maintained by a cross-shelf incision and elongation. Channel bed steepens
160 (channel slope $>1.1\%$), narrows, and thus increased volumes and clast sizes of coarse sediment are transported to
161 the receding shoreline ~~intensify~~ with time (Eyal et al., 2019). Gravels are comprised of carbonates and some chert
162 and their intermediate axes length range between 0.05-0.4 m. From the tributary mouth, the unsorted [bright-color](#),
163 fluvially-derived sediments are ~~then~~ transported northward ~~and~~, sorted along the shore, under winter storm waves
164 ([Figs. 1, 2d](#)). ~~This process was measured, quantified, and modelled at the individual storm scale, determining that~~
165 ~~the coastal longshore sorting is, and are deposited on top of the dark-brown laminated lacustrine deposits of the~~
166 ~~newly exposed lake bed (Figs. 1, 2d). This color distinction between the coarse fluvial-coastal and fine lacustrine~~
167 ~~sediments, along with (i) a direct manifestation of wave climate (Eyal et al., 2021).~~ The interplay between fluvial
168 sediment supply and [subsequent](#) longshore transport during ~~winters~~[winter](#), and ~~significant~~[\(ii\) considerable](#) lake-
169 level decline during ~~summers, results~~[summer, resulting](#) in an annual separation between individual beach berms,
170 which ~~are~~ practically, ~~are~~ fossilized, thus preserving "fossilized" at a certain elevation. [Through correlation with](#)
171 [the well-established lake-level curve, these beach berms are dated to a specific year based on their original coastal](#)
172 ~~sorting~~[elevation \(Ben Moshe et al., 2008; Eyal et al., 2019; Enzel et al., 2022\). The volume of sediment stored in](#)
173 [each of these well-preserved beach berms is approximated to a triangular pyramid geometry \(Eyal et al., 2021\);](#)
174 ~~i.e., 2019). This volume is attributed solely to the fluvially-derived sediments as there is no additional coarse~~
175 ~~sediment contribution from the updrift direction (south) or from nearby gullies draining local muddy areas of the~~
176 ~~shelf. The longshore transport and sorting were measured, quantified, and modelled at the individual storm scale,~~
177 ~~and it was concluded to be a direct manifestation of wave climate (Eyal et al., 2021).~~ ~~reactivation by subsequent~~
178 ~~storm waves of the coastal sediments, as occurs in most shores of earth.~~

179 2.2 Hydroclimate

180 2.2.1 The potential synoptic-scale climatic drivers at the eastern Mediterranean

181 Four major ~~seasonal~~ synoptic systems prevail in the eastern Mediterranean during wind and rain storms that affect
182 the Dead Sea region:

- 183 (i) In winter (mainly December-February), Mediterranean cyclones (MCs) (e.g., Alpert et al., 1990a), also
184 termed Syrian or Cyprus lows, depending on the respective location of their centers, dominate the stormy
185 weather (Alpert et al., 1990a; Alpert and Shay-El, 1994). These extratropical cyclones draw moisture
186 from the Mediterranean and convert it into moderate-intensity rainfall over broad areas (e.g., Ziv et al.,
187 2015; Kushnir et al., 2017). At the regional scale, during the passage of these storms, winds are generally
188 changing from easterlies into westerlies.
- 189 (ii) In autumn (October-December), Red Sea troughs (RSTs) are most common (e.g., Kahana et al., 2002;
190 ~~while~~). While their “active” variant (ARST) generates localized and intense rainfall with high spatial
191 variability (Kahana et al., 2002; Armon et al., 2018, 2019, 2020; Dayan and Morin, 2006; Belachsen et
192 al., 2017; de Vries et al., 2013; Tsvieli and Zangvil, 2007). ~~The~~, the non-active RST usually brings dry
193 easterly winds at the surface (Saaroni et al., 1998).
- 194 (iii) In spring (March-May), Sharav lows are frequent in the southeastern Mediterranean (Northern Egypt and
195 Israel), generating warm and dusty winds (e.g., Alpert and Ziv, 1989) with rarely occurring rains and
196 high-velocity westerly winds following their passage over the area.
- 197 (iv) In summer (June-September), the Persian trough (PT) prevails; low pressure trough extending from the
198 Persian Gulf to the northeast, along with a subtropical high that borders it from the southwest (Alpert et
199 al., 1990b); rainfall is scarce as large-scale atmospheric subsidence dominates the region (Rodwell and
200 Hoskins, 1996; Goldreich, 2003; Kushnir et al., 2017; Tyrlis and Lelieveld, 2013; Lensky and Dayan,
201 2015), and winds are rather consistently flowing from the north-west (e.g., Tyrlis and Lelieveld, 2013;
202 Dayan et al., 2017).

203 2.2.2 The fluvial sediment conveyor

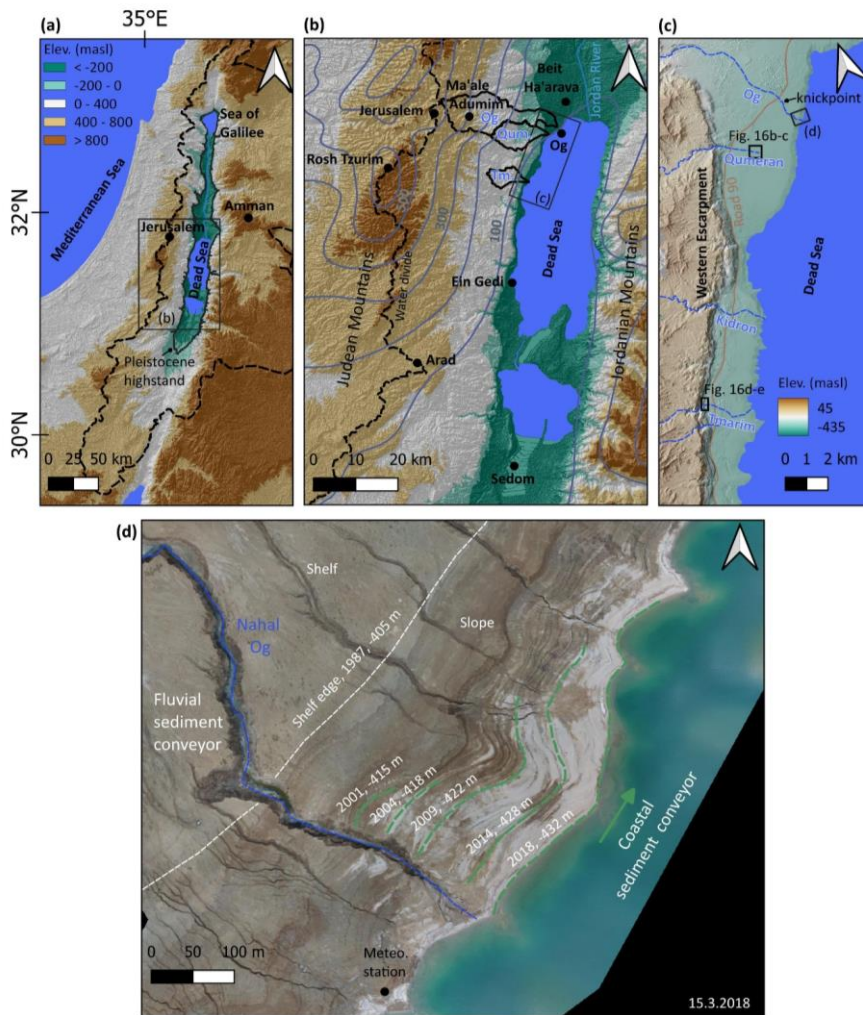
204 Most of the precipitation that produces flash-floods in the Dead Sea region occurs in the heart of the winter,
205 ~~between November to March~~, while the full wet season lasts from October to May (Fig. 3a). Annually, the region
206 experiences approximately 20 MCs during winter and early spring with rainstorms typically lasting 2–3 days
207 (Alpert et al., 2004a; Saaroni et al., 2010) generating relatively high-volume floods (Enzel et al., 2003, 2008;
208 Kushnir et al., 2017; Armon et al., 2018; Shentsis et al., 2012). Smaller number of rainstorms during the autumn
209 and spring are ~~usually~~ associated with ARSTs (Kahana et al., 2002; Armon et al., 2018).

210 The western water divide of the larger Dead Sea tributaries is at the Judean Mountains with peaks up to ~1000
211 meters above sea level (masl) and Mediterranean/semi-arid climate (Fig. 2b). From the water divide eastwards,
212 the topography steeply slopes down to the Dead Sea at elevation of ~437 meters (in 2022) below sea level (mbsl)
213 over a short distance of ~30 km, resulting in a sharp climatic gradient (Fig. 3a) due to the orographic rain-shadow
214 effect (Goldreich, 2003; Kushnir et al., 2017). Thus, streams draining into the Dead Sea from the west are
215 ephemeral and are subjected to flash-floods during sufficient storm rainfall (e.g., Morin et al., 2009). For example,
216 in the Nahal Og watershed (137 km²), the climatic gradient ranges from >500 mm y⁻¹ in the western headwaters
217 to as low as ~50 mm y⁻¹ at the Dead Sea shore (Figs. 2b, 3a). The mean annual total rain volume falling over the
218 basin is ~40x10⁶ m³y⁻¹ (Haviv, 2007; Ben Moshe et al., 2008), of which only a small ~~portion~~ fraction reaches the
219 lake. The highest peak discharge estimated for the stream by high-water marks after the rare flood of 2006, is 330
220 m³ s⁻¹ (Arbel et al., 2009). In Eyal et al. (2019), direct observations of flow marks at a specific location along the
221 channel were interpreted to represent the peak discharge of the common floods of ~20 m³ s⁻¹. Floods, lasting from

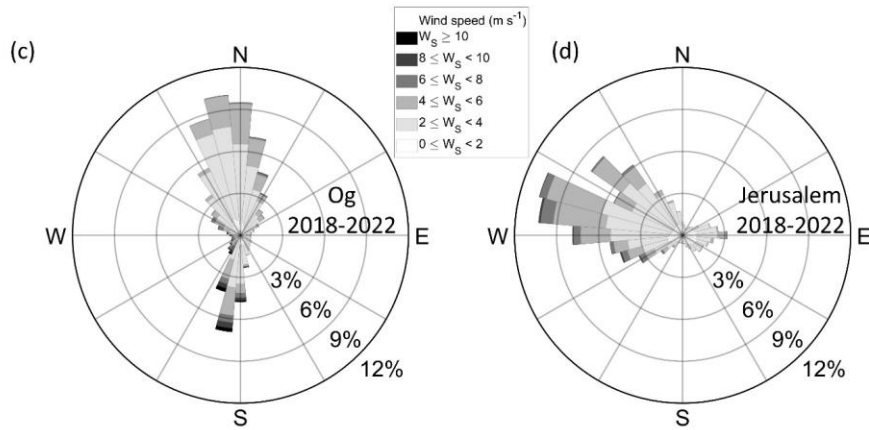
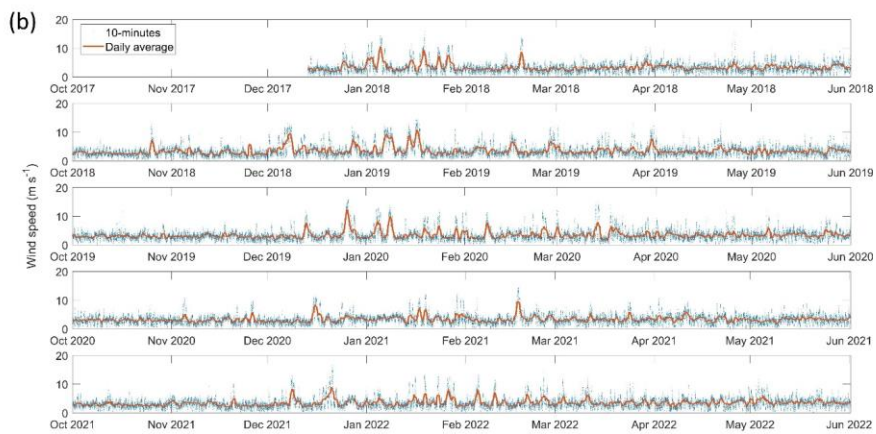
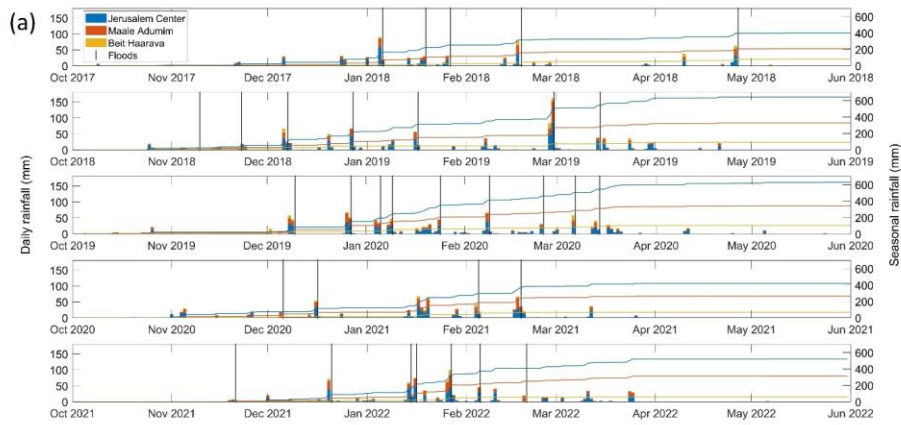
222 a few hours and up to a day, are generally short and ~~quick-responserespond quickly~~ to high-intensity rain (e.g.,
223 Morin et al., 2009).

224 2.2.3 The coastal sediment conveyor

225 Winds along the Dead Sea have a bimodal directional distribution of either northerly or southerly direction (Fig.
226 3b,c) affected by the steep orography and north-south elongation of the Dead Sea rift (Bitan, 1974, 1976; Segal et
227 al., 1983; Vüllers et al., 2018; Kunin et al., 2019). During summer, the diurnal cycle dominates with dry and warm
228 northerly winds ($<10 \text{ m s}^{-1}$) blowing stronger at night-time and weaker during the day, attributed to the meso-
229 scale circulation of the Mediterranean Sea breeze (Alpert et al., 1997; Gertman and Hecht, 2002; Lensky and
230 Dayan, 2012; Lensky et al., 2018; Hamdani et al., 2018; Kunin et al., 2019; Naor et al., 2017). During winter, the
231 diurnal cycle is less dominant as the ~~above-mentioned~~ synoptic scale circulation governs
232 (Hamdani et al., 2018) with southern windstorms, $<20 \text{ m s}^{-1}$, lasting from a few hours to three days, blowing over
233 the $\sim 40 \text{ km}$ south-to-north lake fetch (Eyal et al., 2021). These high-magnitude winter windstorms generate ~~steep~~
234 waves with a maximum height of $\sim 4 \text{ m}$, ~~wave~~-periods of $\sim 4 \text{ s}$, and wavelengths of $\sim 25 \text{ m}$ ~~in~~along the northeastern
235 shores of the Dead Sea (Eyal et al., 2021); ~~the high viscosity\density of the brine (Weisbrod et al., 2016) may~~
236 ~~explain the steepness of the observed wave~~. During storms, waves approach the coast at $\sim 45^\circ$ (Eyal et al., 2021),
237 forming ~~optimum~~optimal conditions for unidirectional longshore drift (Longuet-Higgins, 1970; Van Hijum and
238 Pilarczyk, 1982; Ashton and Giosan, 2011). Along the waterline of the Nahal Og coast, fluvially-derived gravels
239 are distributed over a 20–30 m wide strip, covering the lake floor by a monolayer, extending to a water depth of
240 $\sim 2.5 \text{ m}$; at this depth, ~~a transition~~transitions to sandy-silty wave ripples ~~is~~are documented. The longshore transport
241 and sorting of the coarse gravel and their link to the wave climate were presented in Eyal et al., (2021) for three
242 intensively-monitored storms.



243 Figure 2: Regional setting. (a) The eastern Mediterranean; shown are the Dead Sea watershed (black dashed line) and
 244 the highstand of the Late Pleistocene Lake Lisan, the predecessor of the Dead Sea (black line). (b) The Dead Sea region.
 245 Shown are the regional water divide of the Judean Mountains (dashed black line) and the watersheds of the studied
 246 tributaries: Og (Og), Qumeran (Qum.) and Tmarim (Tm.) (black polygons). Grey contours are isohyets (mean annual
 247 precipitation in mm y^{-1}). They present the rain shadow of the Judean Mountains towards the Dead Sea valley. Black
 248 dots are meteorological stations used in this study. (c) The tributaries draining into the north-western Dead Sea (blue
 249 dashed lines) and the Dead Sea western escarpment. (d) Aerial photograph of the lower reach of Nahal Og emphasizing
 250 the fluvial and coastal conveyors; note the increasing extension farther north, from the stream mouth, of the coastal
 251 gravel with lowering of the lake (green lines). It should be stressed that the tributaries north of Nahal Og drain the
 252 mudflat and do not carry gravel. Modified from Eyal et al., 2021. [We adopt for the Dead Sea margins the global](#)
 253 [terminology of shelf and slope because of their similar geometry \(see Eyal et al., 2019\).](#)



255 **Figure 3: Rainfall and wind forcing during the five, intensively measured hydrological years: December 2017- June**
256 **2022. (a) Daily (bars, left-axis) and seasonal cumulative (lines; right-axis) rainfall measured, from west to east, in**
257 **Jerusalem (blue), Ma'ale Adumim (orange), and Beit-HaArava (yellow), representing the headwaters, the center, and**
258 **lower areas of the watershed, respectively (stations locations are presented in Fig. 2b). Vertical black lines are**
259 **occurrences of floods (Table S1 in the supplement). Note that most storms affect the entire region with consistent decline**
260 **in rainfall amounts away from the water divide. (b) 10-minutes (blue crosses) and daily average (orange line) wind**
261 **speed at Nahal Og mouth. Windrose for (c) Nahal Og (-430 masl) and (d) Jerusalem (835 masl) representing the**
262 **frequency and directionality of winds during the study period. Note the orthogonal wind directions; in the upper**
263 **watershed it is dominated by westerlies, while at the same time, within the Dead Sea rift valley, it is dominated by**
264 **northerlies and southerlies.**

265 3. Methods, data, and [analysisanalyses](#)

266 ~~To We assembled a high-resolution, rich dataset to~~ unfold the chain of processes from ~~the synoptic-scale~~
267 ~~climatology to rainstorms and flood hydrology and~~CPs to wind and wave climate, which are involved in ~~the~~
268 ~~coarse-gravelly sediments along the formation~~coasts of the ~~coastal sedimentary record along this regressive lake,~~
269 ~~we assembled a high-resolution, rich dataset. It~~Dead Sea. The dataset is comprised of: (1) Five-year long,
270 continuous monitoring of winds, waves, lake level, rain and flood hydrology. (2) Storm-scale sediment transport
271 documented in the channel and shore. (3) A combination of this dataset with atmospheric CPs using atmospheric
272 reanalysis. These observations constitute a one-of-a-kind dataset of coeval processes at such a resolution,
273 undoubtedly for this region and probably for elsewhere. Additionally, although these observations are based on
274 only five years of data, ~~comparing a comparison of~~ the rainfall and wind timeseries with ~~records of~~ adjacent long
275 ~~record-term~~ weather stations, indicates that these [five](#) years well represent the mean climatic conditions (Sect. S2
276 in the supplement).

277 3.1 Field measurements

278 *Wind* speed and direction at 10-min intervals were (a) measured at the Nahal Og mouth by a Gill-WindSonic
279 sensor located ~5 m above the lake surface, between December 2017 and June 2022, and (b) obtained from the
280 Israel Meteorological Service for the stations of Jerusalem Center (1999-2022), Ma'ale Adumim (2007-2022),
281 Ein Gedi (2007-2021), Rosh Tzurim (2001-2021), Arad (1999-2021), Sedom (1999-2021) and Beit Ha'arava
282 (2008-2022) (Fig. 2b).

283 *Waves* were measured at 4 Hz frequency by a water pressure sensor (Keller-PAA 36 Xi W) at water depth range
284 of 12 (December 2017) to 8 m (June 2022). Significant wave height and period were analyzed, accounting for the
285 attenuation of wave-induced pressure variation with water depth, and the temporal change of water depth due to
286 lake-level decline (Karimpour and Chen, 2017). From the continuous 4 Hz data, differences between maximum
287 and minimum pressure at 10-min resolution were normalized between 0 (no waves) and 1 (highest observed wave
288 height, $H = 4$ m) and used as proxies for the significant wave height (Fig. S3, Eyal et al., 2021). This was done as
289 the long time-series of 4 Hz measurements is incomplete. This analysis was validated by 16 Hz measurements of
290 RBR-solo-wave pressure sensor, deployed at 5-m water depth during three storm waves.

291 *Rain* data at 10-min intervals were obtained from the Israel Meteorological Service for the stations of Jerusalem
292 Center (1999-2022), Ma'ale Adumim (2008-2022) and Beit Ha'arava (2008-2022).

293 A *Flood Hydrology* data set was gathered from several sources (see Sect. S1 in the supplement), as no direct
294 discharge measurements exist in the watershed: (a) Observations obtained by Time-Lapse Cameras (TLCs) and
295 real-time field surveys, from which hydrographs were estimated using the Manning formula (as in Eyal et al.,
296 2019) (when high flows occurred at night, high water marks were estimated from the daylight video). (b) Flood
297 reports obtained from the Israel Flash-flood Forecasting Center, Water Authority of Israel. (c) Flood reports
298 obtained from the Desert Floods Research Center categorized into no flood, weak flood, moderate flood, and large
299 flood. (d) Social network reports (e.g., Borga et al., 2019), providing an almost complete binary series of yes/no
300 flood occurrences and their estimated magnitude. These observations were synthesized to classify the floods into
301 four categories according to the estimated flood peak-discharge: low-flow floods, which due to transmission losses
302 do not reach the lake, weak floods, moderate floods, and large floods. Estimation of the extremity of the peak
303 discharge for each class was evaluated according to Rinat et al., 2021 (their Fig. 8). Cross-checking between the
304 information sources and close monitoring of the events during the measurement interval of 2017-2022 provides a
305 high level of certainty about the completeness of the flood time series. However, it must be noted that hydrograph
306 estimation gives rough values rather than exact high-resolution measurement data.
307 The *Dead Sea level* was obtained from Water Authority of Israel at a monthly resolution.
308 *Sediment transport* was measured using boulders with masses ranging between 0.5-100 kg. (a) ~~Tens of Many~~
309 ~~(<100)~~ boulders were positioned in the upstream channel ~~before a flood~~ to estimate transport distances ~~by during~~
310 a single ~~event flood~~. (b) ~~Along the beach, using “smart” and Eighty~~ painted boulders ~~and five “smart” boulders~~
311 ~~were positioned along the beach to quantify longshore displacement during individual storm~~, as described in Eyal
312 et al., 2021, ~~for three different storms~~.
313 *Late Pleistocene to modern fan-deltas* were analyzed by: (a) Airborne LiDAR-based DEMs for 2020, with
314 horizontal and vertical resolutions of 0.5 and 0.25 m pixel⁻¹, respectively (obtained from the Geological Survey
315 of Israel). (b) Orthophoto imagery and georeferenced aerial photographs from the years 1945, 1967, 1980, 1987
316 (obtained from the Survey of Israel). (c) A satellite image from 1971 (Corona mission, Grosse et al., 2005; data
317 available from <https://earthexplorer.usgs.gov>) with a spatial resolution of up to several meters per pixel. These
318 images were used to examine landscape change preceding the available LiDAR-based DEMs. They were also
319 used for mapping and determining the altitude of shorelines of the late 20th and 21st centuries, recognized on both
320 air photographs and LiDAR and of Late Pleistocene shorelines in Nahal Tmarim (location in Fig. 2b,c). DEM and
321 hill shade of 30 m pixel⁻¹ resolution obtained from Geological Survey of Israel were used for location maps (Figs.
322 2a,b, and 10a)

323 3.2 Data analysis

324 3.2.1 Storm detection

325 Over 120 storm waves were defined according to a physical threshold of the critical wave height for mobilization
326 of a 1 kg clast: $H_{cr} \approx 0.6$ m as determined previously by Eyal et al., 2021. A one-day interval was selected as
327 ~~separating a separation~~ between individual storms. The timing of storm initiation and cessation was obtained using
328 a lower wave height threshold (e.g., Molina et al., 2019), $H \approx 0.15$ m, which is a sufficiently lower value to account
329 for the entire storm-wave duration (Fig. 4). As the waves are wind-driven (see below Sect. 4), windstorms were
330 defined according to the timing of the storm waves. This was done by applying the timing of the wave initiation
331 and cessation to the wind speed timeseries and redefining the windstorm initiation and cessation according to a

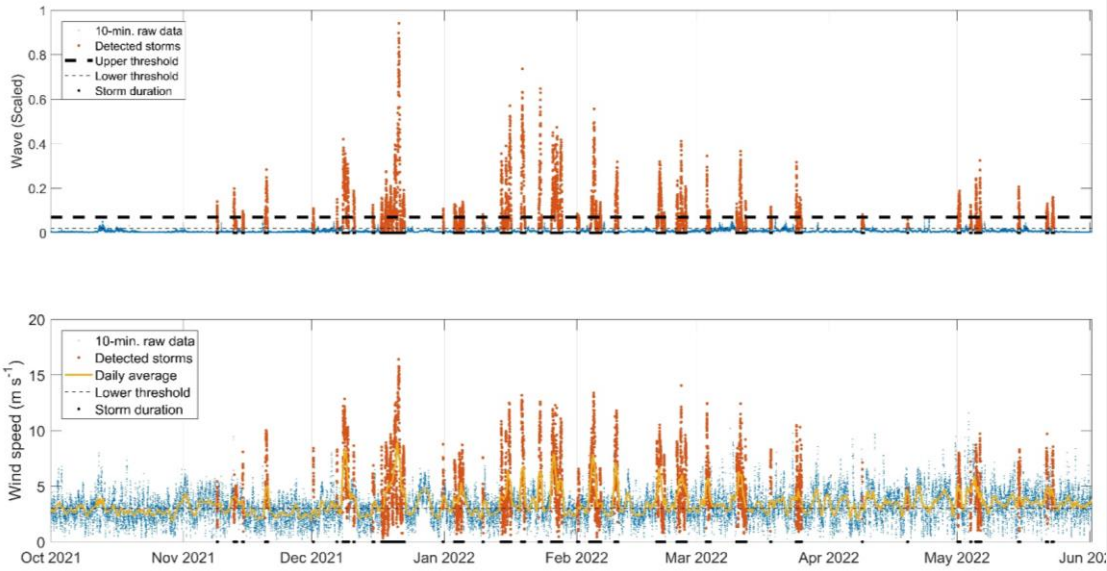
332 wind speed daily mean threshold of 3 m s^{-1} (Fig. 4). This threshold optimally represents the storms following a
333 comparison with a range of thresholds ($0.5 - 5 \text{ m s}^{-1}$). The storm peak is defined as the maximal wind value in the
334 interval between the [windstorm](#) initiation and cessation. Rainfall was analyzed at hourly intervals, accumulated
335 from the 10 minutes data. Thirty-two flood-producing rainstorms were defined by detecting rainstorm peaks using
336 a one-day time interval before and after flood initiation. The timing of rainstorm initiation and cessation were
337 redefined using a 0.1 mm h^{-1} threshold and a separation of at least six hours between successive storms (e.g.,
338 Marra et al., 2020).

339 3.2.2 Synoptic classification

340 We classified wind-waves-rain storms into four classes representing the most common synoptic circulation
341 patterns prevailing in the region (Sect. 2.2.1): Mediterranean Cyclones (MCs), Active Red Sea Troughs (ARSTs),
342 Persian Troughs (PTs), and Sharav Lows (SLs). To do so, we generalized the 19 classes obtained by the semi-
343 objective synoptic classification introduced by [Alpert et al., \(2004b\)](#) for the eastern Mediterranean, which is
344 based on daily (12:00 UTC) meteorological fields at the 1000 hPa pressure level from the NCEP/NCAR reanalysis
345 (2.5° spatial resolution). We classified a storm as a MC if one of the storm days was considered as a MC. ARST
346 was defined if one of the storm days was considered as ARST with no MC prevalence. SL was classified if one
347 of the days during the storm was classified as SL, regardless of the other classes obtained by the semi-objective
348 classification. PT was classified only if it appeared in the summer months between June and September (e.g., Ziv
349 et al., 2004), even if it appeared with other classes. Otherwise, ~~the semi-objective PT~~ was classified as a MC in
350 accordance with weak cyclones manifested as a shallow trough in the ~~north-eastern~~[northeastern](#) Mediterranean
351 (Ziv et al., 2022). ~~The 13 cases classified by the semi-objective classification as highs were manually inspected,~~
352 ~~and were reinterpreted as MCs, as they represent~~[Given that the ending/final stage of MCs is usually characterized](#)
353 [by the dissipation of the low and increased dominance of a high](#) (e.g., Armon et al., 2019;), ~~we decided to manually~~
354 ~~inspect 13 cases in which the semi-objective classification yielded a high. Similar to~~ [Marra et al., \(2021\)-\), we](#)
355 [realized that these cases were actually the final stages of MCs.](#)

356 3.2.3 Composite and individual storm CPs

357 Composite and individual storm CPs were analyzed using data from the European Center of Medium-range
358 Weather Forecasts (ECMWF) Reanalysis model 5 (ERA5; Hersbach et al., 2020). Sea level pressure and 10-m
359 above ground wind maps were produced for the wind-wave storms at their onset, peak and cessation at a resolution
360 of 0.5° per pixel. Composite maps were obtained for (i) the mean conditions during the different storm parts both
361 for all CPs [grouped](#) together and separately for, (ii) the lowest, intermediate, and highest terciles of the wave
362 energy, duration, and wave height, and (iii) the climatology of wave-producing CPs, non-wave-producing CPs,
363 and the anomaly of the wave-producing CP compared to the mean conditions of CP for the same period (2017-
364 2022).



365

366 Figure 4: An example of wind-wave storm detection during one hydrological year (2021-2022). (a) Storm waves (orange
 367 dots) were detected by an upper physical threshold following Eyal et al., 2021 (thick dashed black line), with the full
 368 duration (black dots marked on the x-axis) defined by a lower threshold (thin dashed black line). (b) Windstorms
 369 (orange dots) were defined according to the detected storm waves, with the full duration defined by a lower threshold
 370 (dashed black line) following the daily average of the wind speed (yellow line).

371 4. The fluvial and coastal sediment conveyors and their synoptic-scale hydroclimatic control

372 We present insights from five representative storm-scale case studies in Sect. 4.1 for which we have detailed
373 measurements of sediment transport in the stream and coast under the forcing of atmospheric CPs, winds and
374 waves, rain, and floods (Figs. 5-9). Each component is described with respect to the timeline of a wind-wave
375 storm from its onset, rise, peak, decay, and cessation. Then, in Sect. 4.2, we present the separation of the wind
376 field into two levels with perpendicular directions, i.e., the regional surface wind during storms both outside and
377 inside the Dead Sea rift valley (Fig. 10). In Sect. 4.3 we generalize the processes leading to the activation of the
378 two sediment conveyors with a full analysis of the wind-wave storms and floods of the past five years with their
379 synoptic- and meso-scale climatology (Figs. 11-13). Given that MCs stand out as the main activators of the
380 sediment conveyors (Sect. 4.3 and Fig. 11), we describe the results according to the evolution of this synoptic-
381 scale CP and add information on other CPs when necessary.

382 4.1 The stream and coast at the storm scale

383 4.1.1 Storm-scale atmospheric CPs

384 At the onset of the wind-wave storms, the centers of the MCs are located north of the study region: (i) In the
385 vicinity of Greece, as far as ~1500 km northwest of the Dead Sea (Fig. 5c). (ii) In the eastern Mediterranean near
386 Cyprus, ~500 km northwest of the Dead Sea (Figs. 6-7c). (iii) In Syria or Iraq, 500-700 km north-northeast of the
387 Dead Sea (Fig. 8c). Only seldom storms occur when the cyclone is ~~near~~[nearer to](#) the Dead Sea, in southern Israel
388 (Fig. 9, see a more detailed description of ~~the events~~[such a storm](#) in Dayan et al., (2021) and in Rinat et al., (2021).
389 The prevailing storm circulation is of anti-clockwise westerly/south-westerly winds. Towards the storm peak,
390 MCs focus ~~to~~, i.e., become smaller, ~~and~~ deepen, and move eastwards (Figs. 5-8d). In mature and ending stages of
391 [impacting](#) MCs, the regional westerly flow and lowered inversion (Armon et al., 2019; Goldreich et al., 2004) are
392 manifested by 'mountain waves'; i.e., south-north elongated cloudy crests extending over the Jordanian mountains
393 and plateau (Fig. 6h). The storm is over when the low-pressure systems become larger, shallower, move further
394 to the east, and a high-pressure system invades the region (Figs. 5-8e).

395 4.1.2 Local wind and waves

396 While at the regional scale westerly flows dominates, at the local scale, over the Dead Sea itself, a sharp rise of
397 pronounced southern winds characterizes the onset of storms under MCs as measured along the Dead Sea shores
398 (Figs. 5-9b). With the intensification of the winds to $>10 \text{ m s}^{-1}$ and up to 20 m s^{-1} , northward-propagating waves
399 also intensify (Fig. 5-9b). At the end of the storm, diverse directionality that characterizes the pre- and post-storm
400 intervals of the wind (Figs. 5-9b) prevails, and the wind and waves quickly calm down.

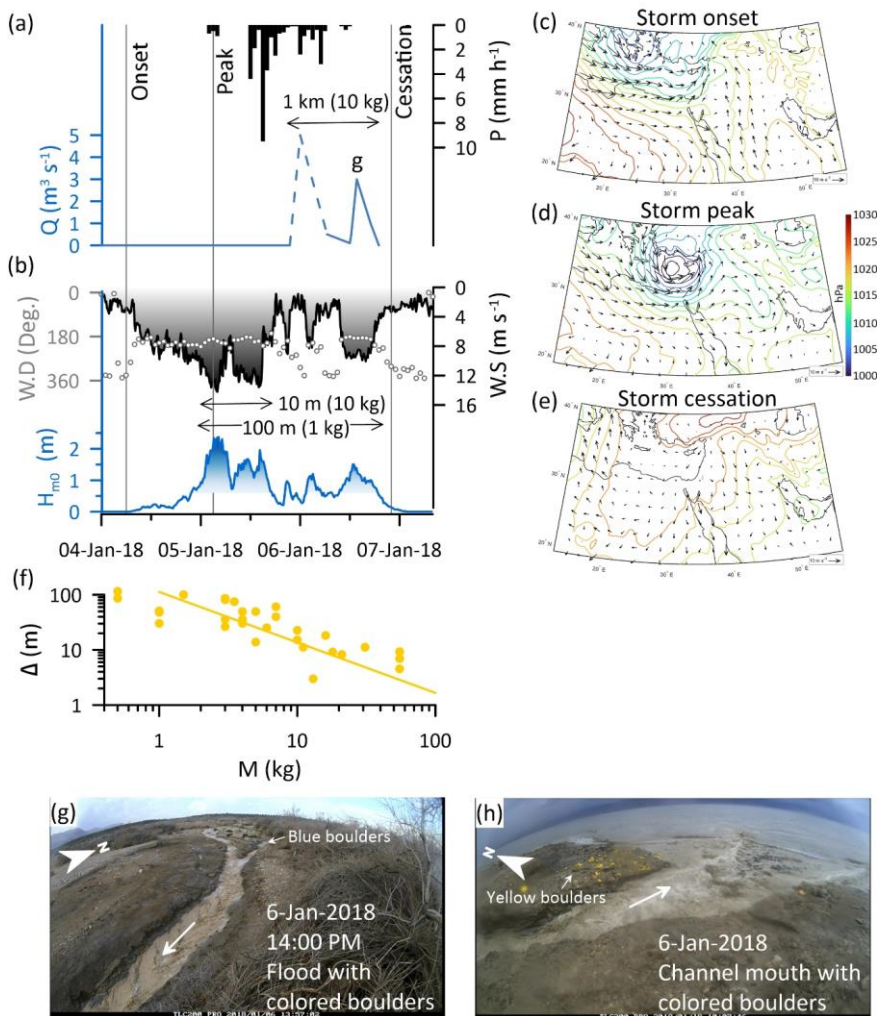
401 4.1.3 Rain and floods

402 Rainfall in the drainage basin (Ma'ale Adumim [station, Fig. 2b](#)) initiates coevally with the wind-wave storms,
403 normally ~~intensifying with intensified rain~~ after ~~or even during the timing of~~ the storm wave peak (Figs. 5, [6a](#), [7-](#)
404 [9a](#)) ~~or even during the peak~~ (Fig. [6a](#)), reaching moderate to high [rainfall](#) intensities relative to this dry climate, of
405 $>5 \text{ mm h}^{-1}$ for the duration of at least [anone](#) hour (Figs. 5-9a). Rainfall intensity may comprise of several maxima,
406 and accordingly, the flash-flood hydrograph presents several peaks (Figs. 5, 7, 8a). Flood discharge ~~ranges~~[maxima](#)

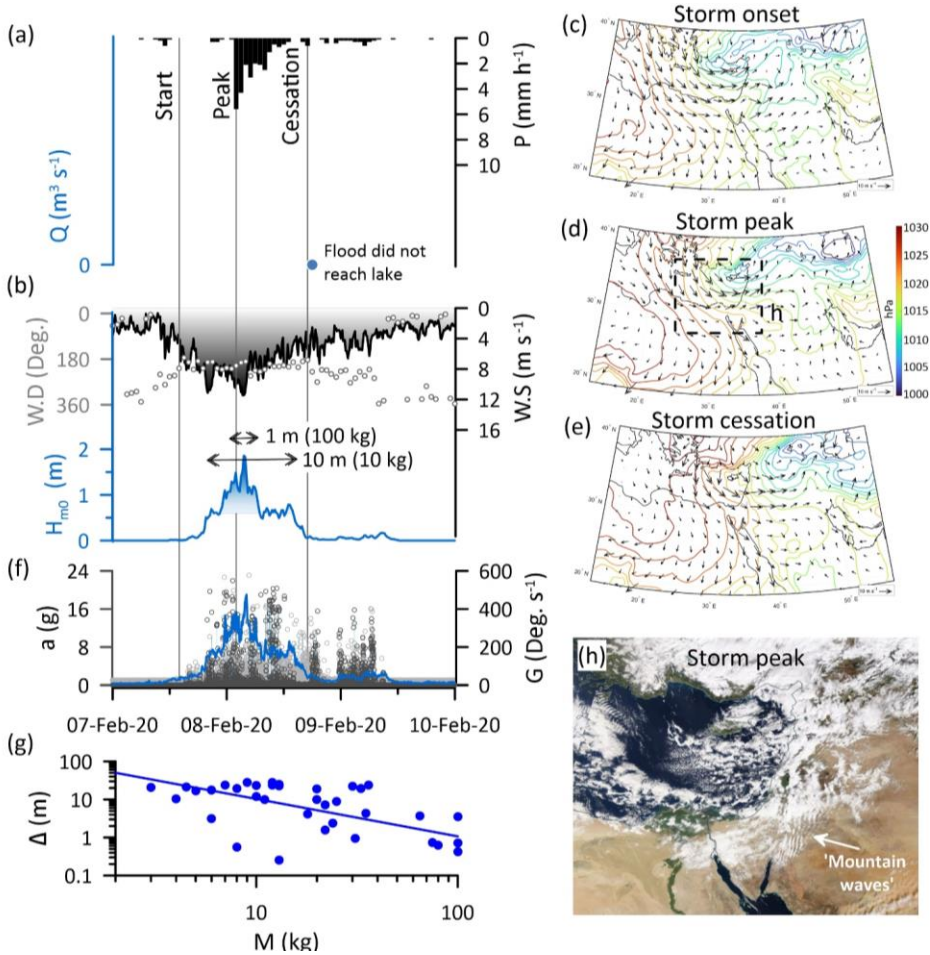
407 range between weak floods ($\sim 5 \text{ m}^3 \text{ s}^{-1}$) (Fig. 5a) and the largest flood documented between 2017-2022, with
408 an estimated peak discharge of $120 \pm 30 \text{ m}^3 \text{ s}^{-1}$ (Fig. 8a). These floods typically last <24 h lagging a few hours after
409 the rain peak; this important observation indicates that sediments are delivered to the stream mouth towards the
410 decay or end of the respective windstorm or storm wave.

411 4.1.4 Sediment transport

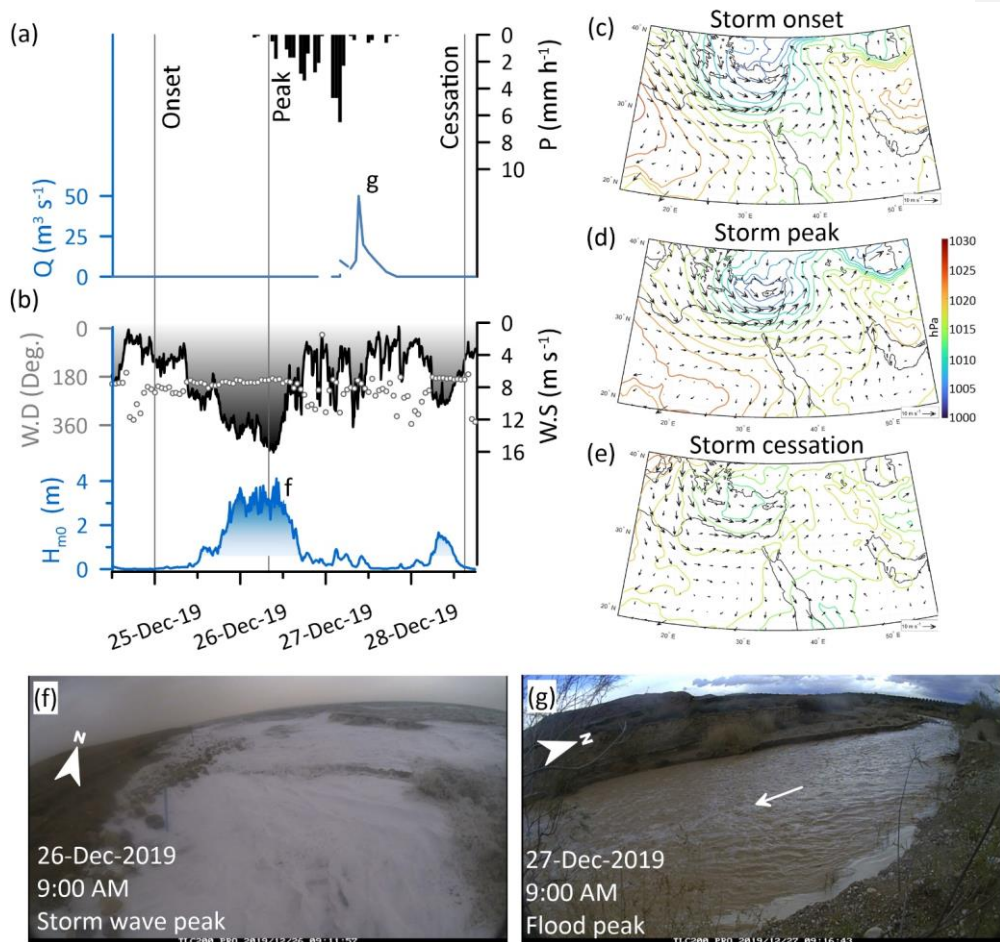
412 With the rise of winds and waves and exceedance of the critical wave height (Fig. 4), certain clasts are mobilized
413 according to their mass as indicated by the recorded, during-storm accelerations and rotations of individual clasts
414 (Fig. 6f, Eyal et al., 2021). During the storm peak, the highest accelerations and rotations are recorded (Fig. 6f).
415 By the end of the storm wave, field observations and measurements indicate that the gravels are sorted along the
416 shore as the displacement decrease with increasing clast mass, according to a power law (Eyal et al., 2021) (Figs.
417 5f, 6g, 9f). Larger During individual storms, larger clasts weighing ten of kilograms are transported to tens of
418 meters, and finer clasts weighing kilograms are transported hundreds of meters along the shore (Figs. 5f, 6g, 9f).
419 Coevally, or by the end of the storm waves, a flood reaches the stream outlet into the Dead Sea (Figs. 5–9a)
420 transporting at a single, relatively low-discharge flood, cobble-boulder sized clasts, up to >10 kg each, along the
421 channel incised channel across the one-kilometer-wide muddy shelf (Fig. 5a). The transport rate of boulders per
422 single event along the shore is one to two orders of magnitudes smaller relative to the transport in the stream. In
423 the common case of floods that are generated after the storm wave, delta deposition and sediment progradation of
424 up to 20 m offshore is were observed at the channel mouth (Fig. 9g-i). In such a case, the storm-scale activity of
425 the coastal conveyor precedes the fluvial conveyor, and longshore transport and sorting of the fluvio-deltaic
426 sediments can only happen during the next storm. A different case is occurs when floods practically do not reach
427 the lake and only the coast is activated by the storm, reworking the sediments delivered by the previous storms in
428 the season (Fig. 6a).



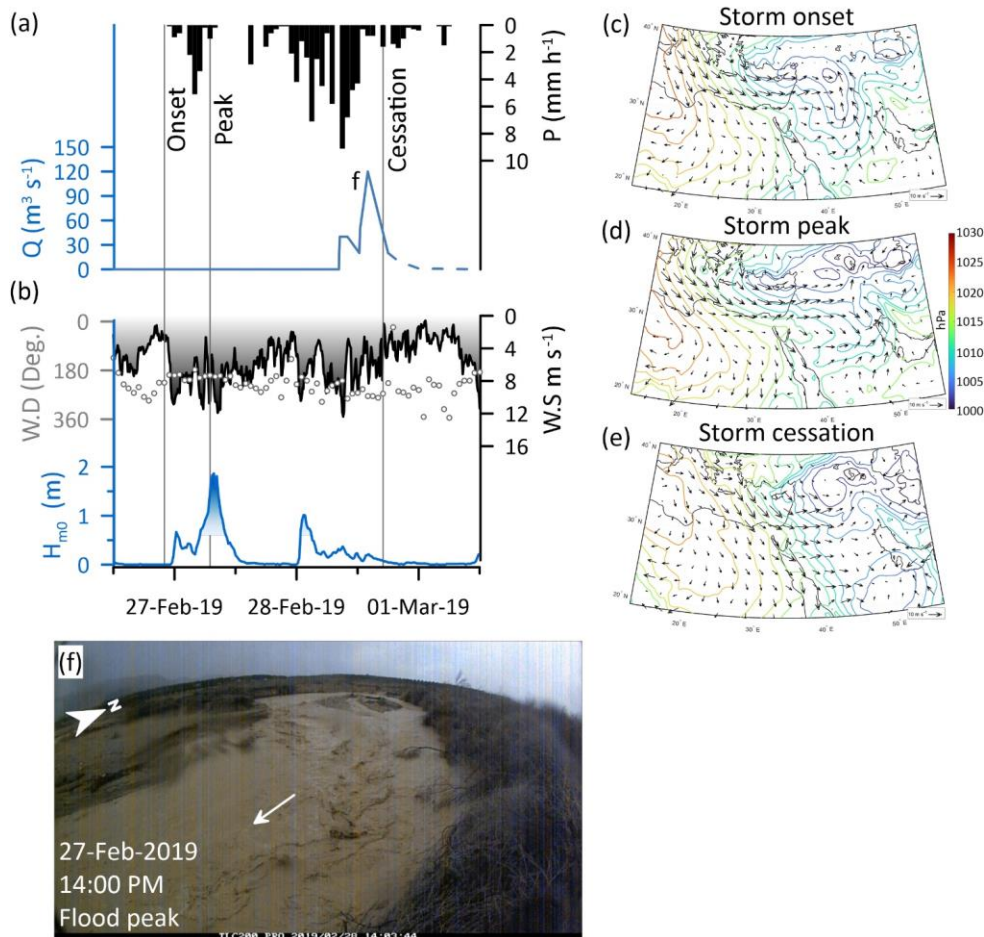
429
 430 Figure 5: Storm-scale observations (4-7 January, 2018) of the chain of processes from the synoptic scale atmospheric
 431 circulation that generate rainstorms-producing floods, wind-wave storms, resulting in fluvial and coastal sediment
 432 transport. (a) Hourly rainfall (P , Ma'ale Adumim, Fig. 2b), flood discharge (Q , solid line based on TLC and dashed
 433 line based on high-water marks). During this flood, colored cobbles-boulders were transported across the entire 1 km
 434 shelf width into the Dead Sea. (b) Wind ($W.S.$ -wind speed, black gradient fill darkens towards higher wind speed, $W.D.$ -
 435 wind direction in dots) and wave height (H -significant wave height, color gradient fill indicates waves above
 436 transport threshold, darkens towards higher waves). (c, d, and e) CP maps of a deep Mediterranean Cyclone plotted
 437 according to the onset, peak, and cessation of wind, respectively. (f) Longshore displacement (Δ) of various-mass
 438 boulders (M) (yellow dots), transported from the channel mouth northward and sorted alongshore according to a
 439 power-law (yellow line), following Eyal et al., 2021. (g) The flood at the stream knickpoint where boulders were colored.
 440 (h) The flood flows into the Dead Sea, where coastal boulders are colored.



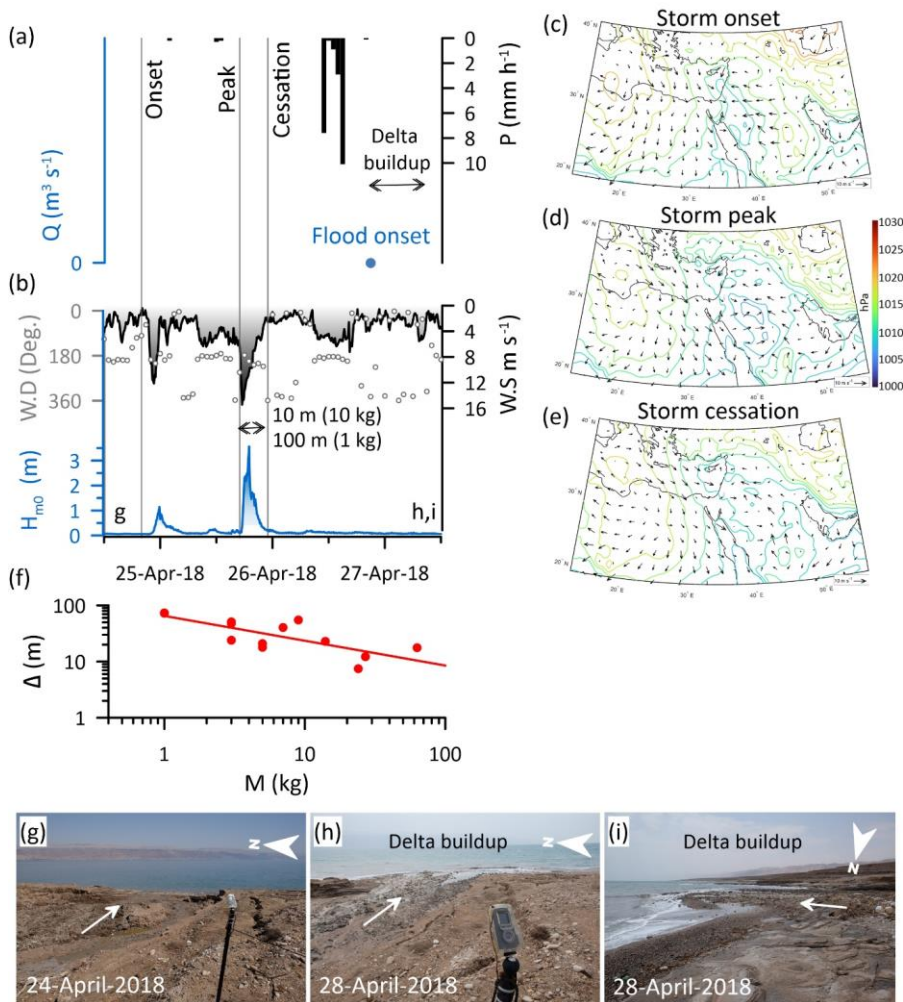
442 Figure 6: Storm-scale observations (7-9 February, 2020) of the chain of processes from the synoptic- scale atmospheric
 443 circulation that generate rainstorms-producing floods, wind-wave storms, resulting in fluvial and coastal sediment
 444 transport. (a) Hourly rainfall (P , Ma'ale Adumim, Fig. 2b), flood was generated but did not reach the lake. The timing
 445 of a first wave is marked by a blue dot. (b) Wind (W.S.-wind speed, black gradient darkens towards higher wind speed,
 446 W.D.-wind direction in dots), and wave height (H -significant wave height, colored/blue gradient fill indicates waves
 447 above transport threshold, darkens towards higher waves). (c, d, and e) CP maps of a Mediterranean Cyclone plotted
 448 according to the onset, peak, and cessation of wind, respectively. (f) Resultant acceleration (a , grey dots) and rotations
 449 (G , black dots) recorded by five, various-mass smart boulders indicating the real-time motions of clasts under storm
 450 waves, following Eyal et al., 2021. (g) Longshore displacement (Δ) of various-mass boulders (M) (blue dots), transported
 451 from the channel mouth northward and sorted alongshore according to a power-law (blue line). (h) Aerial photograph
 452 of the eastern Mediterranean during the storm peak (8 February, 2020) obtained from
 453 <https://worldview.earthdata.nasa.gov/>, location in (d). Note the south-north elongated cloudy crests termed 'mountain
 454 waves', indicating on the synoptic westerly air flow.



455
 456 Figure 7: Storm-scale observations (25-28 December, 2019) of the chain of processes from the synoptic-scale
 457 atmospheric circulation that generate rainstorms-producing floods, wind-wave storms, resulting in fluvial and coastal
 458 sediment transport. (a) Hourly rainfall (P , Ma'ale Adumim, Fig. 2b), flood discharge (Q , solid line-TLC). Wind ($W.S.$ -
 459 wind speed, black gradient darkens towards higher wind speed, $W.D.$ -wind direction in dots) and wave height (H -
 460 significant wave height, colored blue gradient fill indicates waves above transport threshold, darkens towards higher
 461 waves). This storm wave was the largest documented in our record (Video supplement). (c, d, and e) CP maps of a deep
 462 Mediterranean Cyclone plotted according to the onset, peak, and cessation of wind, respectively. (f) The storm wave
 463 during its peak, which is the highest in our record. (g) The flood peak downstream to road 90 (location in Fig. 2c).



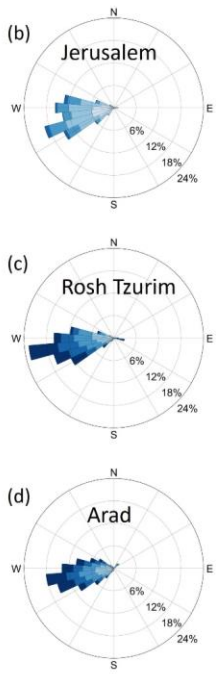
464 Figure 8: Storm-scale observations (27-28, February 2019) of the chain of processes from the synoptic scale atmospheric
 465 circulation that generate rainstorms-producing floods, wind-wave storms, resulting in fluvial and coastal sediment
 466 transport. (a) Hourly rainfall (P, Ma'ale Adumim, Fig. 2b), flood discharge (Q, solid line-TLC). This flood was the
 467 largest documented in our record (Video supplement). (b) Wind (W.S-wind speed, black gradient darkens towards
 468 higher wind speed, W.D-wind direction in dots) and wave height (H-significant wave height, color gradient
 469 indicates waves above transport threshold, darkens towards higher waves). (c, d, and e) CP maps of a Mediterranean
 470 Cyclone centered to the east of the Mediterranean, with an extended trough to the eastern Mediterranean, plotted
 471 according to the onset, peak, and cessation of wind, respectively. (f) The flood peak downstream of Highway 90 (location
 472 in Fig. 2c).



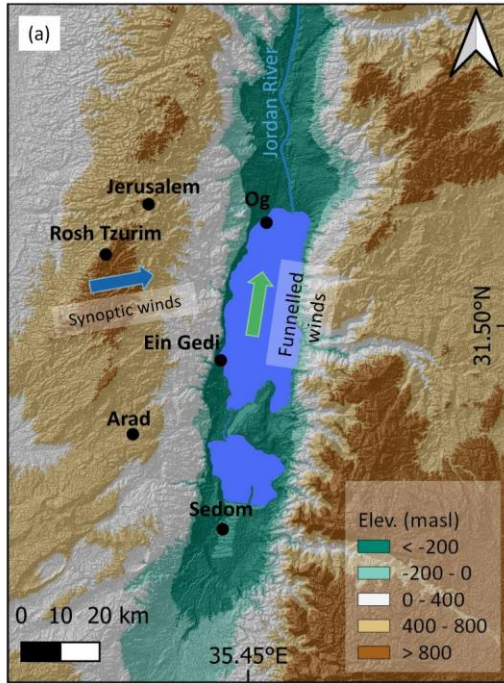
473 Figure 9: Storm-scale observations (25-27 April, 2018) of the chain of processes from the synoptic-scale atmospheric
 474 circulation that generate rainstorms-producing floods, wind-wave storms, resulting in fluvial and coastal sediment
 475 transport. (a) Hourly rainfall (P , Ma'ale Adumim, Fig. 2b). The flood discharge was high, as indicated from a field visit
 476 during this storm. (b) Wind ($W.S$ -wind speed, **black gradient darkens towards higher wind speed**, $W.D$ -wind direction
 477 in dots) and wave height (H -significant wave height, **color gradient darkens towards higher waves**). (c, d, and e) CP maps of a southern-centered Mediterranean Cyclone plotted
 478 according to the onset, peak, and cessation of wind, respectively. This storm also was discussed in detail in Rinat et al.,
 479 (2021) and Dayan et al., (2021). (f) Longshore displacement (Δ) of various-mass boulders (M) (red dots), transported
 480 from the channel mouth northward and sorted alongshore according to a power-law (red line), following Eyal et al.,
 481 2021. (g) The channel mouth before the storm. (h and i) The channel mouth after the flood ends with prominent fan-
 482 delta progradation of ~ 20 m offshore.
 483

484 **4.2 Synoptic-scale and ~~orographically channelled~~topographically funnelled surface winds activating the**
485 **two perpendicular sediment conveyors**

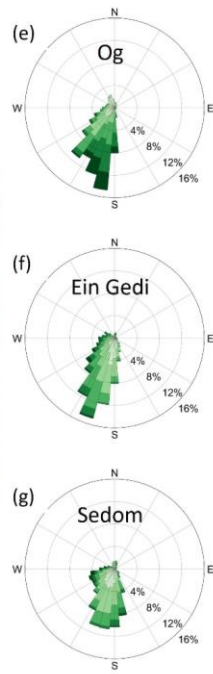
486 During MC storms, synoptic-scale westerly circulation is consistent with measurements of surface wind in ground
487 stations, located along a south-north transect of the 600-1000 masl water divide at the Judean Mountains (Fig.
488 10a-d). Coevally, a transect of the winds within the Dead Sea rift valley at an elevation of ~400 mbsl, ~30 km east
489 of and sub-parallel to the water divide, indicates that the high-magnitude surface winds have a clear southern
490 directionality (Fig. 10a, e-g). We attribute this directionality change, from the regional westerlies into in-rift valley
491 southerlies during the same individual storm, to the orography-funneling effect [by the topography](#) of the Dead
492 Sea valley with its south-to-north oriented rift shoulders (e.g., Bitan, 1976). Consequently, we recognize that the
493 winds associated with the main synoptic-scale circulation pattern (MC) splits into two perpendicular directions;
494 these two hydroclimatic generators activate ~~—differently the coarse-sediment—~~conveyors [of the coarse](#)
495 [sediments](#)(Figs. 1, 10, Video supplement): (i) Westerlies at high altitudes convey moisture from the Mediterranean
496 Sea, with rainfall amounts tending to increase when air parcels encounter the orographic barrier of the Judean
497 Mountains and then decrease [inwhen reaching](#) the rain shadow area of the Dead Sea rift valley (Sharon and Kutiel,
498 1986; Goldreich, 1994; Marra et al., 2022). This orographic effect is an important permanent feature over the last
499 millions of years since the rift reached its shape. This orography determines the amount and distribution of rainfall
500 over the western Dead Sea watersheds and, in turn, the characteristics of floods, and with them the [storm to](#)
501 [seasonal](#) timing of sediment delivery into the basin. The conveyance of moisture continues to the east of the Dead
502 Sea and rainfall amount increases again with the upslope flow over the Jordanian mountains >1000 masl (e.g.,
503 Armon et al., 2019); as a result, floods are generated, and sediments are delivered to the Dead Sea from ~~theits~~
504 eastern watersheds [later or](#) at the very end of the storms. (ii) At the surface, southerlies blow perpendicular to and
505 coeval with the synoptic-scale mountainous winds. The meso-scale funneling of winds blowing over the lake
506 results in south-to-north waves propagation and thus, at the coast, the redistribution of sediments preferentially
507 northwards from the channel mouths along the Dead Sea shores.
508 Weaker CPs have different air trajectories, but as long as the synoptic winds have a slight southern component,
509 the topography and shape of the Dead Sea rift margins govern, resulting in southerly-funneled winds. For example,
510 under ARST conditions, the synoptic-scale wind is southeasterly, while the actual surface wind measurements
511 are pure southerlies (Fig. S4).



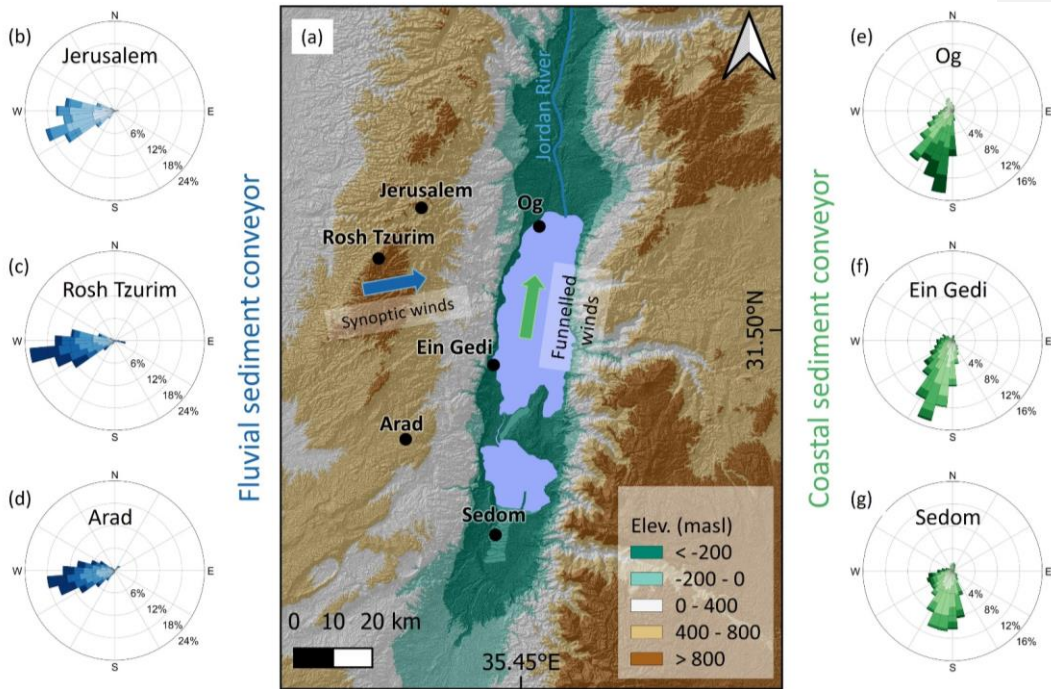
Fluvial sediment conveyor



Coastal sediment conveyor



פ12



513
 514
 515 **Figure 10: Synoptic and meso-scale windstorms.** (a) Location map showing the two perpendicular directions of the
 516 winds flow during MC storms. (b, c, and d) Wind roses from three Judean Mountains water divide stations (locations
 517 are indicated in the map). These data show the western-southwestern high-magnitude winds during winter storms
 518 conveying at high altitudes the moisture for flood generation in the fluvial sediment conveyor (blue coloring). (e, f, and
 519 g) Wind roses from inside the Dead Sea rift valley. These data show the change in wind direction as the synoptic scale
 520 winds are funneled in the rift and transformed into high-magnitude southerlies that generate the northward
 521 propagating storm waves activating the coastal sediment conveyor (green coloring). Legend of the wind roses appear
 522 in Fig. 3c-d.

523 4.3 The sediment conveyors at the seasonal scale under a joint atmospheric circulation generator

524 4.3.1 The coastal conveyor at the seasonal scale

525 Like the stream, the coast is activated mainly between December and March (Fig. 11) under MCs located north
526 of the Dead Sea region (Fig. 12). Each of the 128 classified storm waves (i.e., 10–30 storms per winter) are wind
527 driven and are correlated with high magnitude southern winds (Fig. S6). The wind and wave storm durations are
528 very similar or equal (Fig. 12a), ranging between several hours to three days, <1.5 days for the 25-75 percentiles
529 of the wind (Fig. 13a-b). The prevailing CP during 80% of the identified storms is MC (Fig. 12a), also causing
530 the highest storm wave energy with the longest duration of up to 3.5 days (Fig. S5). At the onset of storms, on
531 average, a deep low-pressure system, ~10 hPa below mean, is located in the vicinity of either Cyprus or Syria,
532 exhibited in the composite ~~analysis and anomaly analyses~~ as bi-center lows in these two regions, and the regional
533 wind direction is western, with a slight southern component over southern Israel (Fig. 13d). At storm ~~waves~~
534 ~~peak wave peaks~~, the ~~area of the~~ low-pressure system contracts ~~its area~~ and ~~the low~~ moves eastwards (Fig. 13e).
535 Along the Dead Sea, the median wind speed at the storms peak is ~~of~~ 10 m s⁻¹ with short-term winds of up to ~~ca.~~
536 20 m s⁻¹ ~~and with~~ a clear southern direction. The wind-driven northwards propagating waves, typically ~~lagging lag~~
537 the regional wind peaks by 0.5-2 h. Median wave height is about ~1 m with maximal height of ~4 m. The cessation
538 of storms is associated with significant shallowing of the MC, appearance of high-pressure system and its
539 advancement from the west, and a change of the mean wind direction into northwesterly winds (Fig. 13f), funneled
540 inside the Dead Sea valley into ~~weaker~~ northerlies.

541 The non-MC storm waves are generated by low wave-energy CPs, mainly by Active Red Sea Troughs, (15% of
542 storm-waves producing CPs). The other 5% are caused by Persian Troughs and Sharav Lows, generating ~~shorter~~
543 storms lasting <10 h (Fig. 12a, Fig. S4). Practically, these storms have a minor impact on the coastal
544 geomorphology and sediment transport as the thresholds (~~as wave height~~) for the motion of clasts in the coastal
545 conveyor are barely exceeded.

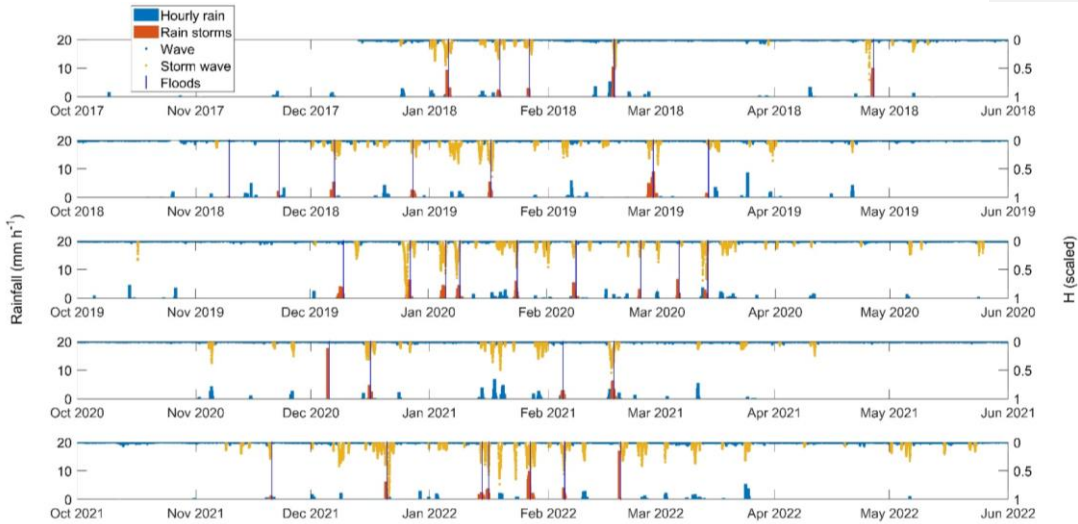
546 The comparison of the mean climatology of wind-wave producing MCs with the nonproducing MCs, show that
547 wind-wave producing MCs ~~are~~: (i) ~~are~~ characterized by stronger regional westerlies, ~~and~~ (ii) ~~have~~ ~3 hPa deeper
548 ~~low at their~~ center, and (iii) ~~accompanied by~~ an adjacent high of ~~ca.~~ +5 hPa higher ~~pressure~~, located over Egypt
549 and Turkey. This ~~total~~ difference of ~8 hPa results in steeper pressure gradients from the north and south of the
550 MC and the generation of stronger winds (Fig. 14), ~~which~~; ~~these winds~~ are ~~then~~ funneled into southerlies at the
551 ~~local-meso~~-scale (Fig. 10).

552 4.3.2 The fluvial conveyor at the seasonal scale

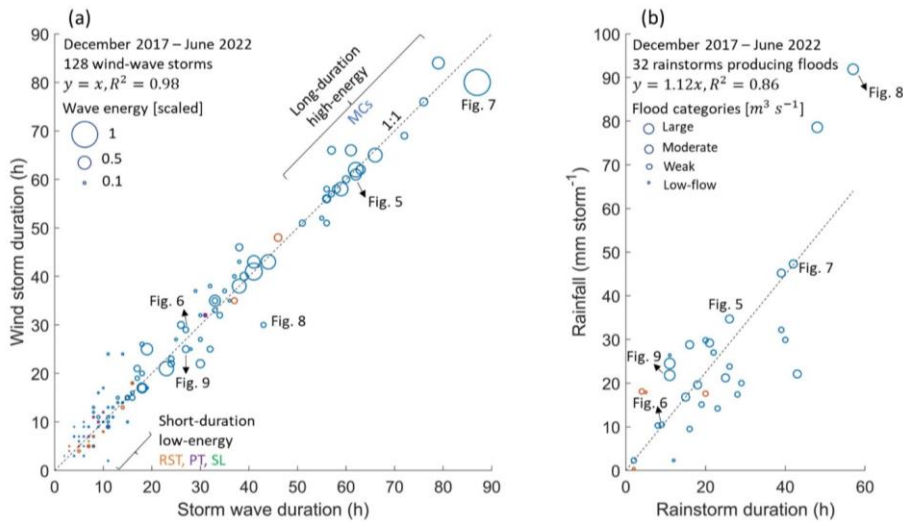
553 Flood-producing rainstorms in the stream occurred 4-9 times per season. Each of these rainstorms lasted between
554 a few hours and up to two days (Figs. 11, 12b) with a typical duration of 10-15 hours for the 25-75 percentiles
555 (Fig. 13c). These rainstorms have a median peak intensity of 5 mm h⁻¹ for the duration of ~~one~~ hour (Fig. 13c),
556 and maximal intensities ~~of up to~~ 20 mm h⁻¹ (Fig. 11). Rain depth >10 mm per ~~such a~~ storm generates moderate
557 or larger floods as measured ~~in at~~ the center of the Nahal Og watershed (Fig. S7). ~~About~~ 60% of the floods present
558 low discharge ~~with a peak discharge~~ (<10 m³s⁻¹) or attenuate to such low flows that the floods ~~practically~~ do not
559 reach the lake. Moderate floods (9 floods, 28%) experience peak discharge of 10–60 m³s⁻¹ and the high-discharge

Formatted: Not Superscript/ Subscript

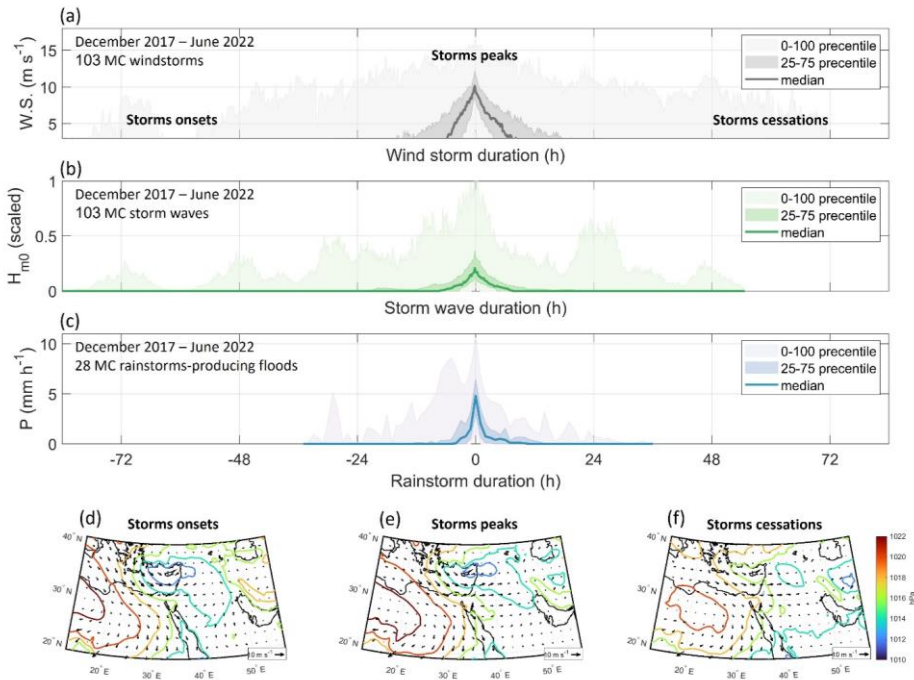
560 floods (4 floods, 12%) have an estimated peak discharge of 60–170 m³s⁻¹. Under rare conditions extreme floods
561 with a peak discharge >170 m³s⁻¹ can be generated. For example, in 2006, an exceptional discharge of 330 m³s⁻¹
562 ~~(was estimated indirectly in Nahal Og based on high-water marks by Arbel et al., (2009); this is~~ equivalent to
563 ~~ana contribution of~~ instantaneous rainfall intensity of 8.7 mm h⁻¹ ~~overfrom~~ the entire watershed, ~~has been~~
564 ~~indirectly estimated in Nahal Og based on high-water marks.~~
565 Approximately 85% of the flood-producing rainstorms were generated by MCs, with all the moderate to large
566 floods generated by this ~~CP-type-circulation pattern (CP)~~. Moreover, these rainstorms occurred coevally with
567 storm waves occurring under the same MCs (Fig. 11). For MCs, rainfall amounts increase with storm duration
568 (Fig. 12b), ~~a relation that an observation~~ we attribute to the characteristically continuous, wide coverage of rainfall
569 during MCs (Armon et al., 2018). The finding is coherent with similar analysis that was applied for the adjacent
570 and ~~much~~ larger Lower Jordan River (Armon et al., 2019).
571 The rest of the flood-producing rainstorms (~15%) are attributed to ARSTs (Fig. 12b). These storms produced
572 low floods during the beginning and end of the hydrological season. This observation emphasizes the control of
573 MCs on geomorphic processes and delivery of sediments to the basin in this region (Fig. 12). For ARSTs, both
574 rainstorm duration and floods occurrence are uncorrelated with rainfall amounts (Fig. 12b); these complex
575 relations are attributed to the short-~~duration-and~~, relatively high-intensity, ~~and~~ localized rainfall associated with
576 ARSTs (e.g., Armon et al., 2018, 2019) that a single rain gauge (Ma'ale Adumim, location in Fig. 2b) cannot
577 capture, biasing the flood-producing rain depth (e.g., Sharon, 1972; Marra and Morin, 2018).



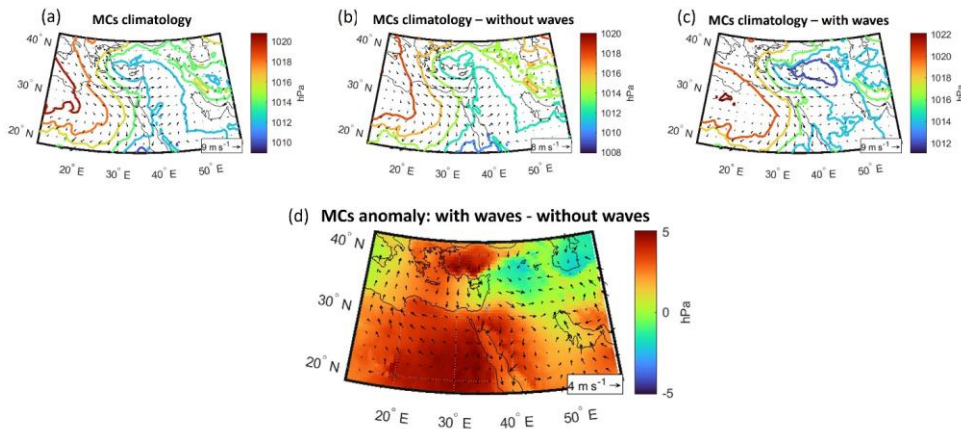
578 **Figure 11: The interaction between fluvial and coastal conveyors during five consecutive hydrological years 2017-2022.**
 579 **Hourly rain depth measured in Ma'ale Adumim (location in Fig. 2b) with classified flood-producing rainstorms (left**
 580 **axis; blue and orange bars, respectively). Vertical blue lines represent the occurrence of floods (Table S1). Waves with**
 581 **classified storm waves (reversed, right-axis; blue and yellow dots, respectively).**



582 **Figure 12: (a) Duration of wind versus wave storms (circles), the energy of a storm wave (circle size), and atmospheric**
 583 **CPs (MC-blue, RST-orange, PT-purple, SL-green). Storm wave energy was calculated for each storm according to**
 584 **$E \sim \sum H_m^2$, and then scaled between 0 to 1 according to the full range of storm wave energies. (b) Rainfall depth versus**
 585 **rainstorm duration at rainstorms-producing floods (circles), the categories of floods (circle sizes), and CPs according**
 586 **to the same color coding as in (a).**



587 Figure 13: The ‘mean’ (a) wind speed, (b) wave height, and (c) flood-producing rainstorms under MCs. Median storms
 588 values (solid lines), intermediate quantiles of the storms (25-75%) and the full range of values (0-100%) is indicated
 589 (shaded-colored areas). Composite mean pressure maps at the (d) onset, (e) peak, and (f) cessation of the wind-wave
 590 storms showing the mean synoptic-scale evolution/climatology during the storms.



591 Figure 14: The climatology and anomaly of MCs producing and non-producing wind-wave storms. MCs climatology
 592 composite pressure maps of (a) all days classified as MC (following Alpert et al., 2004), (b) the non-generating
 593 wind-wave storms, (c) the generating wind-wave storms. (d) The difference (subtraction) between the generating and non-
 594 generating MCs.

595 **5. Hydroclimatic signature in modern ~~to~~and paleo-sedimentary ~~records~~sequences**

596 Following the detailed observations of waves, floods, and related sediment transport under ~~MCs (Mediterranean~~
 597 ~~low-pressure circulation patterns (MC,~~ Sect. 4), we discuss here the accumulation and ~~resulted~~ architecture of
 598 modern and paleo-Dead Sea coastal landforms ~~that were~~ formed over ~~longer~~-time scales of decades to millennia,
 599 ~~i.e., beyond the temporal scales of storms and seasons.~~ In Sect. 5.1, we discuss the accumulation of the Nahal Og
 600 ~~modern~~-recent ~~to modern coarse-delta~~ environment ~~evolving across~~while crossing the Dead Sea shelf and slope
 601 under rapid lake-level fall of the past decades. Then, ~~in~~ Sect. 5.2, ~~we present~~ presents observations of a nearby
 602 stream and its coastal landforms ~~which have~~ accumulated on top of the shelf during the last modern Dead Sea
 603 highstand- (late 19th to earliest 20th century). Finally, in Sect. 5.3, we ~~extend~~use the ~~discussion to~~ gained
 604 insights ~~into the architecture of fan deltas and paleo-beach berms formed during~~in analyzing the ~~map view of a~~
 605 Late Pleistocene ~~coarse-clastic delta and its paleo-beach berms, which formed~~ at the foot of the Dead Sea western
 606 escarpment.

607 **5.1 The evolution of ~~Modern~~modern lowstand coastal berms (at Nahal Og) mouth**

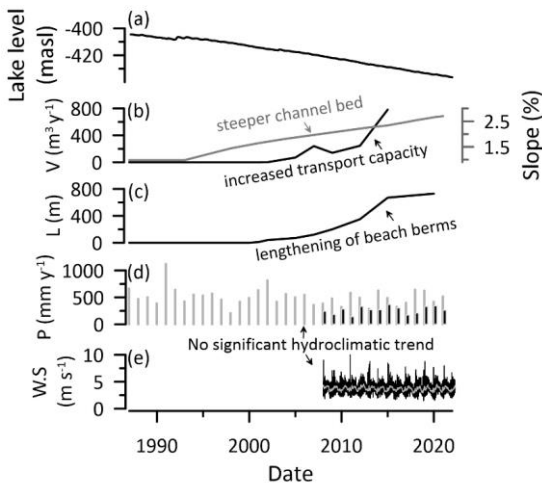
608 The ~~sedimentary record of~~ coarse-clastic beach berms at the Nahal Og mouth ~~has~~have accumulated since the early
 609 2000s (Eyal et al., 2019) (Fig. 2d), pointing to three ~~clear~~ sedimentary/architectural trends over time: (i) Northward
 610 ~~downwind drift of clasts and the~~ deposition of beach berms ~~that,~~ (ii) ~~lengthen with time~~An increase in the length
 611 ~~of beach berms~~ under ~~action of storm-~~waves ~~action,~~ and at the multi-annual scale. (iii) ~~increased~~-Berms show an
 612 ~~increase in~~ sediment volume ~~delivered by the incising and steepening stream to the~~and clast size along receding
 613 ~~shoreline (shorelines (Eyal et al., 2019 and Fig. 15).~~ The northward orientation of deposition is attributed to ~~the~~
 614 ~~abovementioned~~ MCs-generated winter storms and northward propagating waves. However, ~~the latter two these~~
 615 trends ~~contrast the of~~ increased lengthening, volume, and grain-size cannot be explained by trends in the

616 hydroclimatic forcing of winter rain-floods ~~and/or by wind-waves that, these two parameters~~ do not exhibit a
617 ~~significant~~ trend in the past decades (Sect. S2, Fig. 15d-e). If anything, ~~there may be~~ a regional drying trend ~~is~~
618 ~~proposed~~ due to the poleward shift of the storm track and a decrease in total storm rainfall (e.g., Shohami et al.,
619 2011; Zittis et al., 2022; Zappa et al., 2015; Hochman et al., 2018; Armon et al., 2022).

620 Therefore, the ~~increase in sediment volume flux with time should represent~~ intensified sediment delivery to the
621 basin. ~~This~~ is attributed ~~primarily~~ to the ~~geometric response steepening and incision~~ of the channel ~~in response~~ to
622 lake-level fall- (Fig. 15b); ~~it should be noted that the source of the coarse sediments is upstream without any~~
623 ~~sediment contribution by a littoral updrift~~. Following the ~~exposure emergence~~ of the Dead Sea ~~shelf and~~
624 ~~steeperslope from underwater with its ~11% gradient (relatively constant since the late 1980s, Fig. 2d and 5c in~~
625 ~~Eyal et al., 2019), the channel mouth gradients (~40%), asteeptened and~~ rapid incision across the shelf was
626 triggered (Eyal et al., 2019). An expanding knickzone evolved with higher gradients migrating upstream (Ben
627 Moshe et al., 2008), concurrently with channel deepening ~~and narrowing~~ that should increase fluid shear stress
628 exerted on the ~~narrowing~~ channel bed, and ~~therefore, increased~~ bedload sediment flux to the channel mouth
629 (Meyer-Peter and Müller, 1948). Indeed, the transport rate across the shelf for a specific clast size increased over
630 time from tens to hundreds of meters per year over ~15 years (see discussion regarding the ‘virtual velocity’ in
631 Eyal et al., 2019). In larger ~~spatio-temporal~~ ~~spatiotemporal~~ scales, it was shown that channel gradient is a first-
632 order control on sediment supply to river mouths together with the contributing drainage area (Syvitski and
633 Milliman, 2007). The latter factor is dominant along the global ocean shores during glacial periods when global
634 sea level falls and watersheds may merge over the exposed continental shelf (Mulder and Syvitski, 1996;
635 ~~BURGESS~~ ~~Burgess~~ and ~~HOVIUS~~ ~~Hovius~~, 1998), supplying larger volumes of sediment into a certain lowstand
636 delta (e.g., Anderson et al., 2016, for the rivers draining into the Gulf of Mexico). The contribution of climate
637 change during glacial lowstands is considered a second order influencer (Syvitski and Milliman, 2007), with
638 complex relations that may result in either increase or decrease of the sediment delivery to channel mouths (e.g.,
639 Blum and Hattier-Womack, 2009) mainly of the suspended sediment fraction (e.g., Mulder and Syvitski, 1996;
640 Fagherazzi et al., 2004).

641 The lengthening of beach berms with time under ~~annually~~-similar ~~annual~~ wave climate is a less clear phenomenon
642 as it was concluded before that a single clast of a certain mass would travel a fixed, ~~quite~~ predictable distance
643 under a given distribution of wave heights ~~withinduring~~ a storm (Eyal et al., 2021). This raises the question: why
644 would ~~larger~~ ~~annually increasing~~ sediment volumes travel farther along the shore under a similar wave climate?
645 ~~During the early 2000s, when small sediment volumes were delivered to the shore, beach berms of <100 m were~~
646 ~~formed (Fig. 2d, Fig. 15c), whereas between 2018-2022, larger sediment volumes were delivered to the shore and~~
647 ~~gravels were displaced longer distances of hundreds of meters along the shore during single storms (Figs. 5f, 9f).~~
648 Three mechanisms may explain this observation: (i) ~~The decay of wave orbital velocities with~~ ~~Larger sediment~~
649 ~~volume accumulate up to shallower~~ water depth (e.g., Dean and Dalrymple, 1991) ~~results in and are subjected to~~
650 higher near-surface ~~orbital wave~~ ~~breaking-wave~~ orbital velocities, relative to smaller sediment volumes on which
651 ~~lower fluid~~ velocities ~~encountering large, thicker sediment volumes are exerted at a deeper depth~~. Thus, the
652 potential of gravels to travel longer distances along the shore is higher for larger sediment volume. (ii) The
653 ~~increased~~ probability of a clast to be washed out of the swash zone during a storm coevally to the dominating
654 stormy longshore transport (e.g., Benelli et al., 2012). Lighter/smaller clasts have a higher probability to be washed
655 out of the swash zone than heavier/larger clasts that tend to travel down the beach slope under the influence of

656 gravity (e.g., Grotto et al., 2015). Consequently, smaller sediment volumes, characterized by smaller grain-clast
 657 size distributions (Eyal et al., 2019), have a higher probability to be washed completely be washed-out of the
 658 swash zone at the early stages of the season, forming shorter-extending beach berms. (iii) ReworkingCross-shore
 659 down-slope flux of coarse sediments between beach berms between successive years. Lake-The lake level
 660 declines at a decline of ca. 1.2 m y⁻¹ currently operates over the relatively steep (~10%), ~11%, beach slope,
 661 exposing annually ca. one half (10-15 m) of the 20-to-30-m wide strip of the previous year coastal sediment,
 662 leaving coarse sediments that are deposited alongshore. Thus, <50% of the coarse sediment remains submerged
 663 underwater. This way, sediments that have travelled with a potential to further move along the shore in the
 664 previous year, during the following winters. Such sediments start moving to move from an advanced advanced
 665 downdrift location, and reach reaching farther northward distances. This inter-annual process cross-shore sediment
 666 flux is superimposed on the existing signal of increasing fluvial sediment volumes volume flux conveyed to the
 667 coast with time. Gravels weighing several kilograms travel distances of hundreds of meters during single storms
 668 between 2018-2022 (Figs. 5f, 9f), an order of magnitude longer distance than the shortest beach berm preserved
 669 in the Nahal Og from the early 2000s with a length of tens of meters (Fig. 2d). This observation strengthens the
 670 assertion that for larger volumes of sediment, gravels are displaced farther along the shore, and the inter-annual
 671 recycling between beach berms, may be superimposed on the signal of beach berms lengthening with time.



685 Figure 15: Reorganization and the buildup of lowstand sedimentary record under hydroclimatic forcing. (a) Dead Sea
 686 lake level. (b) Average channel slope of Nahal Og, measured between Highway 90 to the Dead Sea (Fig. 2c), increase
 687 with time in response to rapid level decline (right axis; grey), the estimated increase in annual volume flux of
 688 sediment (V) delivered to the channel mouth following Eyal et al., (2019) (left axis; black). (c) Increase in the length (L)
 689 of beach berms with time. (d) Annual rainfall (P) in Ma'ale Adumim (black bars, 2008-2022) and Jerusalem (grey bars,
 690 1985-2022). (e) Wind speed (W.S) in Beit Ha'Arava (black line; daily mean, grey line; monthly mean, 2008-2022).

691 It was demonstrated that the plan-view sedimentation geometry and the channel orientation of wave-dominated
 692 deltas are controlled by feedbacks between the directional wave climate, fluvial sediment supply, and alongshore
 693 sediment bypassing (Nienhuis et al., 2016, their Figure 4); relatively low fluvial and littoral-updrift sediment
 694 supply support the asymmetry in the deposition of deltas with channels evolving in the downdrift direction. In the

695 mouth of Nahal Og, alongshore transport by waves occurs over five times more frequently than the delivery of
696 sediments by moderate and larger floods (Sect. 4), i.e., the potential longshore sediment transport is by far larger
697 than the stream sediment input (Nienhuis et al., 2015); This indicates that a deltaic depocenter cannot evolve and
698 the sediments are transported and deposited downdrift alongshore. We attribute the perpendicular alignment of
699 the channel mouth with the shoreline (Figure 2d) to the absence of updrift sediment contribution. Additionally,
700 according to Nienhuis et al. (2016), under constant wave climate (Fig. 15e) and an increase in the fluvial sediment
701 supply (Fig. 15b), the deltaic shorelines architecture should become more symmetric with time. However,
702 continuous and rapid lake-level fall results in the separation of annually fluvially-derived sediment packages;
703 instead of accumulating at the same elevation in front of the channel mouth with the shoreline changing its
704 orientation, sediments are transported laterally away from the channel mouth and are deposited along individual
705 shorelines at different elevations.

707 5.2 Modern highstand coastal landforms of a nearby stream (Nahal Qumeran)

708 The northward elongation of beach berms deposited during the highstand phase of the early 20th century Dead Sea
709 at the mouth of a nearby ephemeral stream, Nahal Qumeran (Fig. 16a-c) provides a wider perspective of our
710 analysis. The Nahal Qumeran catchment ~~neighbors~~ is neighboring Nahal Og from the south (Fig. 2b,c), ~~it has a~~.
711 It is smaller (47 km²) and drier ~~watershed with~~ mean annual rain volume over its watershed of $8 \times 10^6 \text{ m}^3 \text{ y}^{-1}$ (Ben
712 Moshe et al., 2008) ~~is, by far, lower than the Nahal Og-~~ ~~watershed that tap the wetter zone of the Judean mountains~~
713 (Fig. 2). Between 1945 to 1960 the Dead Sea level was relatively stable, ranging between -390 to -395 mbsl, and
714 Nahal Qumeran was fluvially connected to the Dead Sea shores through a braided coarse-clastic fan-delta. During
715 the 1960s and 1970s, with the onset of human-induced lake-level decline, the stream ~~could keep~~ ~~was keeping~~ pace
716 with the slowly regressive shoreline to feed its highstand fan-delta (Fig. 16b,c). During this interval, a series of
717 beach berms, similar to those ~~formed~~ ~~observed~~ in Nahal Og, were formed, ~~showing extension;~~ ~~these berms are also~~
718 ~~extended~~ to the north from the Nahal Qumeran channel mouth, fitting the above--detected preferred directionality
719 of winter winds and storm waves (Sect. 4). We do not identify any trends of increased sediment volumes or
720 lengthening of beach berms in the channel mouth ~~as of the Nahal Qumeran, probably because~~ its base level ~~is~~
721 ~~approximately~~ ~~was quite~~ stable and the channel profile and sediment flux ~~are~~ ~~were~~ not interrupted. ~~Since~~ ~~A change~~
722 ~~is noted at~~ the early 1970s, ~~when the~~ lake-level decline has accelerated; ~~at this stage,~~ the Qumeran channel ~~did~~ ~~was~~
723 not ~~able to~~ keep pace with the rapid receding shoreline and ~~the~~ low-gradient mudflats emerged (see also Eyal et
724 al., 2019; Enzel et al., 2022). At that moment, Nahal Qumeran stopped responding to the rapid lake-level decline
725 and ~~became~~ disconnected from the lake, showing no incision across the shelf or any sediment delivery to the lake
726 (Eyal et al., 2019). Instead, this stream maintains the buildup of an alluvial fan prograding onto the mudflat
727 platform, ~~with no substantial impacts of~~ ~~without a noticeable impact by~~ the lake coastal hydrodynamics that
728 ~~generate~~ ~~has generated~~ the northward depositional asymmetry, related to the regional forcing of MCs. It seems that
729 as long as the fluvial and coastal conveyors ~~interact~~ ~~interacted at the Nahal Qumeran,~~ regional hydroclimatology
730 was manifested in northward elongating beach berms, similar to Nahal Og. However, disconnecting the fluvial
731 from the coastal conveyors, ~~transforms~~ ~~transformed~~ the channel mouth from a fan-delta into an alluvial fan that
732 develops onto the mudflats regardless of the water body hydrodynamics.

5.3 Late Pleistocene Lake Lisan - sedimentary record of Nahal Tmarim

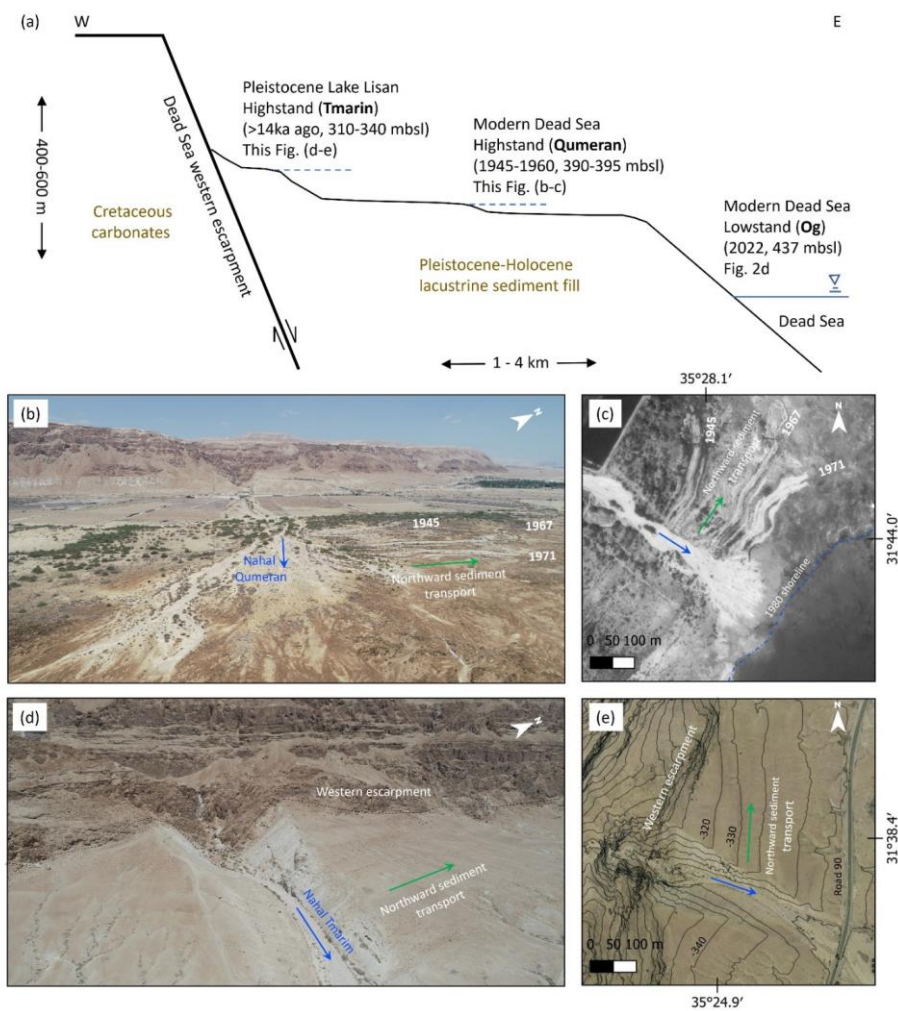
Following the observations from the modern Dead Sea in Nahal Og and Nahal Qumeran, we explore whether the control of southern winds along the Dead Sea rift valley, had affected past deltaic-coastal sedimentary morphology. At the foot of the western Dead Sea escarpment at stream outlets [there are well-preserved](#), Gilbert-type fan-deltas, alluvial fans, and paleo-shorelines [including beach berms that are](#) associated with the higher [levels and recession-stands](#) of the Late Pleistocene Lake Lisan [are well-preserved and its latest Pleistocene recession](#) (Fig. 16a,d,e; see Fig 2b for the extent of Lake Lisan) (e.g., Manspeizer, 1985; Frostick and Reid, 1989; Bowman, 1971, 2019); [Enzel et al., 2022](#)). We have recognized [a noticeable](#) asymmetry in the deposition of fan-deltas [along most and shoreline features at the exits of the northwestern shores of the Dead Sea in both](#) large and small streams [from the northwestern Dead Sea escarpment](#); they present preferential deposition and more pronounced shorelines north ([vs. south](#)) of the feeding canyon mouths (Sect. S7). Channel outlets from the ~~Deas~~Dead Sea escarpment/cliff [are basically bedrock canyons and, therefore,](#) maintain their locations since the Late Pleistocene [as successions](#), Successions of Lake Lisan deposits are preserved inside deeply incised canyons at stream banks (e.g., Bartov et al., 2007) [indicating this stable outlets](#). Thus, the depositional geometry and asymmetry of the channel deposits are evaluated with respect to the channel outlet from the Dead Sea escarpment as an indicator of their deposition due to funneled wind and wave storm direction in the Late Pleistocene. Here we present [an one](#) example from the outlet of Nahal Tmarim (~22 km² drainage area), located ~15 km south of Nahal Og (Fig. 2b,c). Its Pleistocene fan-delta and its recessional paleo-shorelines/beach berms are deposited at elevations ranging between 310 to ~~330~~350 mbsl, [in part](#) corresponding to [lake level decline of the](#) Late Pleistocene to Holocene [lake-level decline](#) (e.g., Bartov et al., 2007; Torfstein and Enzel, 2017). The depositional configuration shows the abovementioned asymmetry, with most of the sediment volume of the fan-delta extends northward of the stream outlet from the cliff (Fig. 16d,e); the surface area of deposits north of the channel outlet is four times larger than the ~~depositional~~[respective](#) area south of the outlet. Furthermore, sorting of cobbles-boulders is observed along the paleo-shorelines; [of Nahal Tmarim, where](#) clast ~~sizes decrease~~[size decreases](#) northward and away from the Tmarim channel outlet, whereas, practically, no shorelines/berms are recognized south of the stream outlet. The [present-day](#) fan-delta of ~~current~~ Nahal Tmarim is different from the modern fan-deltas of Nahal Og and Nahal Qumeran in several aspects: (i) It is a thick (20-30 m) deposit with Gilbert-type forests and paleo-shorelines, [are](#) preserved on its surface. (ii) There is some [additional](#) contribution of coarse materials to the coastal system either directly [throughby](#) the [nearby](#) cliff taluses or by [local](#) debris flows occurring under exceptionally heavy storms (David-Novak et al., 2004; Ahlborn et al., 2018). (iii) ~~The Nahal Tmarim delta~~ [was built during Lake Lisan highstand and got its final geomorphic shape but was also shaped](#) during the regression of the lake (27-14 ka ago) and the transition into the Holocene ~~conditions~~, [14 \(sometimes between 20-12 ka ago \(e.g., Bowman, 2019\)\)](#). Despite these dissimilarities, the framework under which this sedimentary record had evolved with the northward extension of the delta, [is seems](#) similar. ~~It indicates a dominating~~[In both cases, modern and Late Pleistocene, observations agree with the domination of](#) southern wind-wave regime and [aits](#) signature ~~on past sedimentary records during the latest Pleistocene, were very similar to today in the morphology and sediment distribution~~.

The highest stand of Lake Lisan ca. 26,000 years ago reached 145-165 ~~mbsl~~[meters below sea level](#) (Bowman and Gross, 1992; Bartov et al., 2002; Abu Ghazleh and Kempe, 2009), and extended over 240 km, from the Sea of Galilee to the northern Arava (e.g., Bartov 2007) (Fig. 2a). The potential length of the fetch ~~at what is, which~~ currently [encompass the length of](#) the northern Dead Sea basin ~~more than doubled from,~~ but only for southerly

774 winds, was much larger during the high stand for the current northern Dead Sea basin. This is correct for both ~~the~~
775 ~~north~~northern and ~~the south~~southern winds blowing into the study area from the northern and southern edges of
776 Lake Lisan. Thus, both northerlies, presently driven by meso-scale circulation of Mediterranean Sea breeze (e.g.,
777 Lensky et al., 2018), and southerlies, mainly driven by synoptic-scale MCs, could have potentially generated
778 waves high enough to transport gravels along the shores of the lake in both directions. However, the observed
779 preferential deposition asymmetry points to the southerlies control, and in turn, to MCs that generated these
780 southerlies-driven-waves with transport of coarse gravels northward; ~~there is now~~ we did not identify evidence for
781 a preferred fetch from the north.

782 Moreover, the northward directional organization of coarse sediments in the basin agrees with the increased
783 frequency of MCs during wetter intervals of high lake stands in the Dead Sea basin (Armon et al., 2019; Enzel et
784 al., 2003, 2008; Ben Dor et al., 2018). This inference is based on present-day climatology showing that wetter
785 winters and high-lake levels are characterized by higher frequencies of deeper and southerly displaced storm
786 tracks of MCs (e.g., Ben Dor et al., 2018; Enzel et al., 2008, 2003; Saaroni et al., 2010). Prevalence of more
787 frequent, deeper MCs during the wetter Late Pleistocene, should have been resulted in an intensified activation of
788 ~~both~~ the fluvial and coastal sediment conveyors, compared with modern conditions, as MC is the only CP that can
789 generate both rainstorms and windstorms in this region. Floods were more intense and probably more frequent;
790 (Ben Dor et al., 2018), they have delivered amplified sediment fluxes into the basin (Bartov et al., 2007).
791 Westerlies/southwesterlies funneled in the rift valley into southerlies were more frequent and intensified, blowing
792 over a longer lake fetch of diluted/fresher and less dense water, thus potentially generating higher amplitude
793 waves, with ~~maximum~~-heights that exceeded the maximum modern ~~4-m~~-height of four meters. Such waves are
794 characterized by higher fluid orbital velocities that generate higher forces ~~to transport~~capable of transporting larger
795 boulders for longer distances along the coast.

796



797 Figure 16: Modern and paleo-northward-extending beach berms and fan deltas. (a) Schematic cross section from the
 798 western Dead Sea escarpment to the modern Dead Sea showing the stratigraphic/geomorphic location of the three
 799 geomorphic records discussed in the paper. For location of the sites see Fig. 2b-c. (b) Angular drone photograph of
 800 Nahal Qumeran, and (c) orthophoto of Nahal Qumeran (1980), both showing the northward extending beach berms
 801 deposited as long as the stream fed the earlier 20th century shorelines with sediments. Since lake level decline has
 802 accelerated, the stream did not keep pace with the receding shore and an alluvial fan begun developing on top of the
 803 exposed shelf. (d) Angular drone photograph of Nahal Tmarim, and (e) orthophoto of Nahal Tmarim (2012), both
 804 showing the norward deposition of fan-delta and beach berms under late Pleistocene Lake Lisan wind-wave regime.
 805 The asymmetry of sediment deposition to the north is evident also by looking at the elevation contours in (e), converging
 806 with steps of pleo-shorelines, with respect to the escarpment strike; northward of the channel, contours are sub-parallel
 807 to the escarpment direction, whereas they diagonally approach it on the southern part.

808 6. Summary and conclusions

809 Mediterranean cyclones (MCs) are the main synoptic-scale generators of both rain and storm waves over the Dead
810 Sea region. Thus, they are also the main drivers for the coarse-clastic fluvial sediment flux into the lake and the
811 transport and sorting of clasts along shores. First, these MCs generate the high-magnitude [more persistent](#) synoptic
812 wind with westerly cyclonic circulation propagating to the northeastern Mediterranean. Near the surface and
813 perpendicular to this synoptic wind direction, the flow is funneled ~~orographically~~[topographically](#) along the Dead
814 Sea rift valley into southerlies that generate waves activating the *coastal conveyor*. Then, when the cyclone
815 position migrates closer to the eastern Mediterranean shoreline or is centered inland ~~in~~[over](#) Syria, the northern
816 component of the wind becomes more prominent, the southerly wave-producing winds decay, and rainfall evolves
817 in the watershed over the Judean Desert. The rainfall generates floods, which activate the *fluvial conveyor* within
818 a few hours. Thus, fluvial sediments reach the basin either coevally with or completely after the decay of the storm
819 waves. Accordingly, the longshore transport and sorting often occurs during the next storm ~~in~~[usually within](#) the
820 same season, or infrequently, over the same cyclonic system.

821 MCs-producing waves are, on average, ~10 hPa deeper, generating southern winds of up to 20 m s⁻¹ that last >10
822 hours. When the wind-driven waves are higher than 0.6 m, [which is](#) the threshold for ~~transport of~~[transporting](#) a 1-
823 kg clast, the coastal conveyor is activated ~~and gravelly beach berms are formed~~. When rainfall of >10 mm per
824 storm accumulates at the center of the watershed, moderate ~~flood~~ or larger [floods](#) are likely to activate the fluvial
825 conveyor.

826 Although both the stream and coast are usually activated under MCs, the transport under storm waves is >five
827 times more frequent than the delivery of sediments by moderate or larger floods. This is geomorphologically
828 noticeable in the wave-dominated fan-delta, transformed into regressive beach berms extending northward of the
829 Nahal Og mouth. As the ~~flood hydroclimatology shows~~[hydroclimatic parameters that characterized floods show](#)
830 no clear trend in recent decades, the increase of sediment volume [and clast size](#) delivered to the channel mouth
831 during this interval, ~~is~~[are](#) attributed [here](#) to the response of the stream profile to base-level fall, ~~the~~[The](#) exposed
832 stream mouth is steep and ~~result~~[results](#) in incising, steepening, and in increased bedload transport capacity.
833 Concurrently, under rather constant wave climate, this increase in sediment discharge is associated with longer
834 transportation distances of coarse gravels along the shore, and the increase of the beach berms length with time.

835 Guided by the observation from modern environments, we recognized ~~that a~~ similar directionality ~~of the~~
836 ~~hydroclimatology resulted in~~[in Late Pleistocene](#) sedimentary deposition northward of canyon mouths in fan-deltas
837 and coastal deposits ~~from the Late Pleistocene~~. This [may imply similar synoptic scale hydroclimatic drivers also](#)
838 [in the past](#). This, in turn, implies that over past [several](#) millennia, MCs have played [the](#) major role in connecting
839 fluvial delivery of coarse sediments, and their distribution in the lake and along its coasts.

840 7. Data availability

841 The data related to this work is available on Mendeley Data repository
842 <https://data.mendeley.com/drafts/65bhpwfrth> (Eyal et al., 2022), and in Table S1 in the supplement. Rain gauge
843 data were provided and pre-processed by the Israel Meteorological Service (<https://ims.data.gov.il/>; they are freely
844 available in Hebrew only). ERA5 data can be downloaded from <https://cds.climate.copernicus.eu> (Hersbach et al.,

Formatted: English (United Kingdom)

845 2020). Flood reports from the years 2019-2022 were obtained from the Desert Floods Research Center
846 (<https://floods.org.il/english/>; they are freely available in Hebrew only).

847 **8. Video supplement**

848 The videos related to this article are available on <https://photos.app.goo.gl/rLysYEfoVSzyGdQo7>.

849 **9. Supplement link**

850 **10. Author contribution**

851 HE, MA, and NGL conceptualized this work. The methodology was developed by HE, MA, and NGL. Data
852 curation and formal analyses were performed by HE and MA. Funding was acquired by NGL, YE, and HE. NGL
853 and YE supervised the work. HE wrote the original draft of this paper, which was reviewed and edited by all
854 authors.

855 **11. Competing interests**

856 The authors declare that they have no conflict of interest.

857 **12. Acknowledgements**

858 This study was funded by the following grants: PI-NGL: ISF-1471/18, BSF-2018/035, NSF-BSF-2019/637; PI-
859 YE: ISF-946/18. HE is grateful to the Azrieli Foundation for the Azrieli Fellowship. MA was supported by an
860 ETH Zürich Postdoctoral Fellowship (Project No. 21-1 FEL-67), by the Stiftung für naturwissenschaftliche und
861 technische Forschung and the ETH Zürich Foundation. We thank Vladimir Lyakhovsky, Eckart Meiburg, Efrat
862 Morin and Itai Haviv for discussions and insights. We acknowledge Ziv Mor, Ido Sirota, Raanan Bodzin, Uri
863 Malik and Hallel Lutzky for the assistance in the field and laboratory and Liran Ben Moshe for the drone
864 photography. Dorita Rostkier-edelstein and Lida Shendrik are acknowledged for providing the updated synoptic
865 classifications following Alpert et al., 2004, and Yoav Levi for sharing the large IMS datasets of rain and wind.

866 **13. References**

- 867 Abu Ghazleh, S. and Kempe, S.: Geomorphology of Lake Lisan terraces along the eastern coast of the
868 Dead Sea, Jordan, *Geomorphology*, 108, 246–263, <https://doi.org/10.1016/j.geomorph.2009.02.015>, 2009.
- 869 Ahlborn, M., Armon, M., Ben Dor, Y., Neugebauer, I., Schwab, M. J., Tjallingii, R., Shoqeir, J. H.,
870 Morin, E., Enzel, Y., and Brauer, A.: Increased frequency of torrential rainstorms during a regional late
871 Holocene eastern Mediterranean drought, *Quat. Res.*, 89, 425–431, <https://doi.org/10.1017/qua.2018.9>, 2018.
- 872 Alpert, P. and Shay-El, Y.: The moisture source for the winter cyclones in the EM, *Isr. Meteorol. Res.*
873 *Pap.*, 5, 20–27, 1994.
- 874 Alpert, P. and Ziv, B.: The Sharav Cyclone: Observations and some theoretical considerations, *J.*
875 *Geophys. Res.*, 94, 18495, <https://doi.org/10.1029/JD094iD15p18495>, 1989.
- 876 Alpert, P., Neeman, B. U., and Shay-El, Y.: Climatological analysis of Mediterranean cyclones using
877 ECMWF data, *Tellus A Dyn. Meteorol. Oceanogr.*, 42, 65–77, <https://doi.org/10.3402/tellusa.v42i1.11860>,
878 1990a.
- 879 Alpert, P., Abramsky, R., and Neeman, B. U.: The prevailing summer synoptic system in Israel—
880 subtropical high, not Persian trough, *Isr. J. Earth Sci.*, 39, 93–102, 1990b.
- 881 Alpert, P., Shafir, H., and Issahary, D.: Recent changes in the climate at the Dead Sea—a preliminary
882 study, *Clim. Change*, 37, 513–537, <https://doi.org/https://doi.org/10.1023/A:1005330908974>, 1997.
- 883 Alpert, P., Osetinsky, I., Ziv, B., and Shafir, H.: A new seasons definition based on classified daily
884 synoptic systems: an example for the eastern Mediterranean, *Int. J. Climatol.*, 24, 1013–1021,
885 <https://doi.org/10.1002/joc.1037>, 2004a.
- 886 Alpert, P., Osetinsky, I., Ziv, B., and Shafir, H.: Semi-objective classification for daily synoptic
887 systems: application to the eastern Mediterranean climate change, *Int. J. Climatol.*, 24, 1001–1011,
888 <https://doi.org/10.1002/joc.1036>, 2004b.
- 889 Amit, R. and Gerson, R.: The evolution of holocene reg (gravelly) soils in deserts: An example from
890 the dead sea region, *CATENA*, 13, 59–79, [https://doi.org/10.1016/S0341-8162\(86\)80005-4](https://doi.org/10.1016/S0341-8162(86)80005-4), 1986.
- 891 Anderson, J. B., Wallace, D. J., Simms, A. R., Rodriguez, A. B., Weight, R. W. R., and Taha, Z. P.:
892 Recycling sediments between source and sink during a eustatic cycle: Systems of late Quaternary northwestern
893 Gulf of Mexico Basin, *Earth-Science Rev.*, 153, 111–138, <https://doi.org/10.1016/j.earscirev.2015.10.014>, 2016.
- 894 Arbel, S., Getker, M., Arazi, A., Yosi, B., Moshe, G., Efraim, F., and Alon, M.: Data of rain and floods
895 of exceptional events in the hydrological year 2006–2007, special report M-84, 2009.
- 896 Armon, M., Dente, E., Smith, J. A., Enzel, Y., and Morin, E.: Synoptic-Scale Control over Modern
897 Rainfall and Flood Patterns in the Levant Drylands with Implications for Past Climates, *J. Hydrometeorol.*, 19,
898 1077–1096, <https://doi.org/10.1175/JHM-D-18-0013.1>, 2018.
- 899 Armon, M., Morin, E., and Enzel, Y.: Overview of modern atmospheric patterns controlling rainfall
900 and floods into the Dead Sea: Implications for the lake’s sedimentology and paleohydrology, *Quat. Sci. Rev.*,
901 216, 58–73, <https://doi.org/10.1016/j.quascirev.2019.06.005>, 2019.
- 902 Armon, M., Marra, F., Enzel, Y., Rostkier-Edelstein, D., and Morin, E.: Radar-based characterisation
903 of heavy precipitation in the eastern Mediterranean and its representation in a convection-permitting model,
904 *Hydrol. Earth Syst. Sci.*, 24, 1227–1249, <https://doi.org/10.5194/hess-24-1227-2020>, 2020.
- 905 Armon, M., Marra, F., Enzel, Y., Rostkier-Edelstein, D., Garfinkel, C. I., Adam, O., Dayan, U., and

906 Morin, E.: Reduced Rainfall in Future Heavy Precipitation Events Related to Contracted Rain Area Despite
907 Increased Rain Rate, *Earth's Futur.*, 10, e2021EF002397, <https://doi.org/10.1029/2021EF002397>, 2022.

908 Ashton, A. D. and Giosan, L.: Wave-angle control of delta evolution, *Geophys. Res. Lett.*, 38, n/a-n/a,
909 <https://doi.org/10.1029/2011GL047630>, 2011.

910 Ashton, A. D., Hutton, E. W. H., Kettner, A. J., Xing, F., Kallumadikal, J., Nienhuis, J., and Giosan,
911 L.: Progress in coupling models of coastline and fluvial dynamics, *Comput. Geosci.*, 53, 21–29,
912 <https://doi.org/10.1016/j.cageo.2012.04.004>, 2013.

913 Bárdossy, A. and Filiz, F.: Identification of flood producing atmospheric circulation patterns, *J.*
914 *Hydrol.*, 313, 48–57, <https://doi.org/10.1016/j.jhydrol.2005.02.006>, 2005.

915 Bartov, Y., Stein, M., Enzel, Y., Agnon, A., and Reches, Z.: Lake Levels and Sequence Stratigraphy of
916 Lake Lisan, the Late Pleistocene Precursor of the Dead Sea, *Quat. Res.*, 57, 9–21,
917 <https://doi.org/10.1006/qres.2001.2284>, 2002.

918 Bartov, Y., Goldstein, S. L., Stein, M., and Enzel, Y.: Catastrophic arid episodes in the Eastern
919 Mediterranean linked with the North Atlantic Heinrich events, *Geology*, 31, 439, [https://doi.org/10.1130/0091-7613\(2003\)031<0439:CAEITE>2.0.CO;2](https://doi.org/10.1130/0091-7613(2003)031<0439:CAEITE>2.0.CO;2), 2003.

920
921 Bartov, Y., Bookman, R., and Enzel, Y.: Current depositional environments at the Dead Sea margins as
922 indicators of past lake levels, in: *New Frontiers in Dead Sea Paleoenvironmental Research*, vol. 401, Geological
923 Society of America, 127–140, [https://doi.org/10.1130/2006.2401\(08\)](https://doi.org/10.1130/2006.2401(08)), 2006.

924 Bartov, Y., Enzel, Y., Porat, N., and Stein, M.: Evolution of the Late Pleistocene Holocene Dead Sea
925 Basin from Sequence Stratigraphy of Fan Deltas and Lake-Level Reconstruction, *J. Sediment. Res.*, 77, 680–692,
926 <https://doi.org/10.2110/jsr.2007.070>, 2007.

927 Belachsen, I., Marra, F., Peleg, N., and Morin, E.: Convective rainfall in a dry climate: relations with
928 synoptic systems and flash-flood generation in the Dead Sea region, *Hydrol. Earth Syst. Sci.*, 21, 5165–5180,
929 <https://doi.org/10.5194/hess-21-5165-2017>, 2017.

930 Benelli, G., Pozzebon, A., Bertoni, D., and Sarti, G.: An RFID-Based Toolbox for the Study of Under-
931 and Outside-Water Movement of Pebbles on Coarse-Grained Beaches, *IEEE J. Sel. Top. Appl. Earth Obs.*
932 *Remote Sens.*, 5, 1474–1482, <https://doi.org/10.1109/JSTARS.2012.2196499>, 2012.

933 [Ben Dor, Y., Armon, M., Ahlborn, M., Morin, E., Erel, Y., Brauer, A., Schwab, M. J., Tjallingii, R.,](https://doi.org/10.1038/s41598-018-25969-6)
934 [and Enzel, Y.: Changing flood frequencies under opposing late Pleistocene eastern Mediterranean climates. *Sci.*](https://doi.org/10.1038/s41598-018-25969-6)
935 [Rep.](https://doi.org/10.1038/s41598-018-25969-6), 8, 8445, <https://doi.org/10.1038/s41598-018-25969-6>, 2018.

936 [Ben Moshe, L., Haviv, I., Enzel, Y., Zilberman, E., and Matmon, A.: Incision of alluvial channels in](https://doi.org/10.1016/j.geomorph.2007.03.014)
937 [response to a continuous base level fall: Field characterization, modeling, and validation along the Dead Sea.](https://doi.org/10.1016/j.geomorph.2007.03.014)
938 [Geomorphology](https://doi.org/10.1016/j.geomorph.2007.03.014), 93, 524–536, <https://doi.org/10.1016/j.geomorph.2007.03.014>, 2008.

939 Bitan, A.: The wind regime in the north-west section of the Dead-Sea, *Arch. für Meteorol. Geophys.*
940 *und Bioklimatologie Ser. B*, 22, 313–335, <https://doi.org/10.1007/BF02246585>, 1974.

941 Bitan, A.: The influence of the special shape of the dead-sea and its environment on the local wind
942 system, *Arch. für Meteorol. Geophys. und Bioklimatologie Ser. B*, 24, 283–301,
943 <https://doi.org/10.1007/BF02263460>, 1976.

944 Blum, M. D., Martin, J., Milliken, K., and Garvin, M.: Paleovalley systems: Insights from Quaternary
945 analogs and experiments, *Earth-Science Rev.*, 116, 128–169, <https://doi.org/10.1016/j.earscirev.2012.09.003>,

946 2013.

947 [BLUMBlum](#), M. D. and [HATTIER-WOMACKHattier-Womack](#), J.: Climate Change, Sea-Level

948 Change, and Fluvial Sediment Supply to Deepwater Depositional Systems, in: External Controls of Deep-Water

949 Depositional Systems, SEPM (Society for Sedimentary Geology), 15–39,

950 <https://doi.org/10.2110/sepmsp.092.015>, 2009.

951 [Bookman, R., Enzel, Y., Agnon, A., and Stein, M.: Late Holocene lake levels of the Dead Sea. Geol.](#)

952 [Soc. Am. Bull., 116, 555–571, https://doi.org/https://doi.org/10.1130/B25286.1, 2004.](#)

953 Bookman, R., Bartov, Y., Enzel, Y., and Stein, M.: Quaternary lake levels in the Dead Sea basin: two

954 centuries of research, *Geol. Soc. Am. Spacial Pap.*, 401, 155–170, [https://doi.org/10.1130/2006.2401\(10\).For](https://doi.org/10.1130/2006.2401(10).For),

955 2006.

956 Borgia, M., Comiti, F., Ruin, I., and Marra, F.: Forensic analysis of flash flood response, *WIREs Water*,

957 6, e1338, <https://doi.org/10.1002/wat2.1338>, 2019.

958 Bowman, D.: Geomorphology of the shore terraces of the late pleistocene Lisan lake (Israel),

959 *Palaeogeogr. Palaeoclimatol. Palaeoecol.*, 9, 183–209, [https://doi.org/10.1016/0031-0182\(71\)90031-9](https://doi.org/10.1016/0031-0182(71)90031-9), 1971.

960 Bowman, D.: The Regional Approach: Alluvial Fans along the Dead Sea-Arava Rift Valley, in:

961 *Principles of Alluvial Fan Morphology*, Springer Netherlands, Dordrecht, 135–151, [https://doi.org/10.1007/978-](https://doi.org/10.1007/978-94-024-1558-2_19)

962 [94-024-1558-2_19](https://doi.org/10.1007/978-94-024-1558-2_19), 2019.

963 Bowman, D. and Gross, T.: The highest stand of Lake Lisan: ~ 150 meter below MSL, *Isr. J. Earth-*

964 *Sciences*, 41, 233–237, 1992.

965 Bowman, D., Banet-Davidovich, D., Bruins, H. J., and Plicht, J. Van der: Dead Sea shoreline facies

966 with seismically-induced soft-sediment deformation structures, Israel, *Isr. J. Earth Sci.*, 49, 197–214,

967 <https://doi.org/10.1560/GXHT-AK5W-46EF-VTR8>, 2000.

968 Bowman, D., Svoray, T., Devora, S., Shapira, I., and Laronne, J. B.: Geomorphology Extreme rates of

969 channel incision and shape evolution in response to a continuous , rapid base-level fall , the Dead Sea , Israel,

970 *Geomorphology*, 114, 227–237, <https://doi.org/10.1016/j.geomorph.2009.07.004>, 2010.

971 Bridge, J. S.: The interaction between channel geometry, water flow, sediment transport and deposition

972 in braided rivers, *Geol. Soc. London, Spec. Publ.*, 75, 13–71, <https://doi.org/10.1144/GSL.SP.1993.075.01.02>,

973 1993.

974 [BURGESSBurgess](#), P. M. and [HOVIUSHovius](#), N.: Rates of delta progradation during highstands:

975 consequences for timing of deposition in deep-marine systems, *J. Geol. Soc. London.*, 155, 217–222,

976 <https://doi.org/10.1144/gsjgs.155.2.0217>, 1998.

977 Coleman, J. M. and Prior, D. B.: Deltaic environments of deposition, in: *M 31: Sandstone Depositional*

978 *Environments*, AAPG Special Volumes, 139–178, 1982.

979 David-Novak, H. Ben, Morin, E., and Enzel, Y.: Modern extreme storms and the rainfall thresholds for

980 initiating debris flows on the hyperarid western escarpment of the Dead Sea, Israel, *Geol. Soc. Am. Bull.*, 116,

981 718, <https://doi.org/10.1130/B25403.2>, 2004.

982 Dayan, U. and Morin, E.: Flash flood–producing rainstorms over the Dead Sea: A review, in: *New*

983 *Frontiers in Dead Sea Paleoenvironmental Research*, vol. 401, Geological Society of America, 53–62,

984 [https://doi.org/10.1130/2006.2401\(04\)](https://doi.org/10.1130/2006.2401(04)), 2006.

985 Dayan, U., Ricaud, P., Zbinden, R., and Dulac, F.: Atmospheric pollution over the eastern

986 Mediterranean during summer – a review, *Atmos. Chem. Phys.*, 17, 13233–13263, [https://doi.org/10.5194/acp-](https://doi.org/10.5194/acp-17-13233-2017)
987 17-13233-2017, 2017.

988 Dayan, U., Lensky, I. M., Ziv, B., and Khain, P.: Atmospheric conditions leading to an exceptional
989 fatal flash flood in the Negev Desert, Israel, *Nat. Hazards Earth Syst. Sci.*, 21, 1583–1597,
990 <https://doi.org/10.5194/nhess-21-1583-2021>, 2021.

991 ~~Dean, R. G. and Dalrymple, R. A.: *Water Wave Mechanics for Engineers and Scientists*, WORLD~~
992 ~~SCIENTIFIC, https://doi.org/10.1142/1232_1991.~~

993 Dente, E., Lensky, N. G., Morin, E., Grodek, T., Sheffer, N. A., and Enzel, Y.: Geomorphic Response
994 of a Low-Gradient Channel to Modern, Progressive Base-Level Lowering: Nahal HaArava, the Dead Sea, *J.*
995 *Geophys. Res. Earth Surf.*, 122, 2468–2487, <https://doi.org/10.1002/2016JF004081>, 2017.

996 Dente, E., Lensky, N. G., Morin, E., Dunne, T., and Enzel, Y.: Sinuosity evolution along an incising
997 channel: New insights from the Jordan River response to the Dead Sea level fall, *Earth Surf. Process.*
998 *Landforms*, <https://doi.org/10.1002/esp.4530>, 2018.

999 Dente, E., Lensky, N. G., Morin, E., and Enzel, Y.: From straight to deeply incised meandering
1000 channels: Slope impact on sinuosity of confined streams, *Earth Surf. Process. Landforms*, 46, 1041–1054,
1001 <https://doi.org/10.1002/esp.5085>, 2021.

1002 ~~Ben Dor, Y., Armon, M., Ahlborn, M., Morin, E., Erel, Y., Brauer, A., Schwab, M. J., Tjallingii, R.,~~
1003 ~~and Enzel, Y.: Changing flood frequencies under opposing late Pleistocene eastern Mediterranean climates, *Sci.*~~
1004 ~~*Rep.*, 8, 8445, <https://doi.org/10.1038/s41598-018-25969-6>, 2018.~~

1005 Elliot, T.: *Deltas*, edited by: Reading, H., Oxford, 113–154 pp., 1986.

1006 Enzel, Y. and Bar-Yosef, O.: *Quaternary of the Levant*, edited by: Enzel, Y. and Bar-Yosef, O.,
1007 Cambridge University Press, <https://doi.org/10.1017/9781316106754>, 2017.

1008 Enzel, Y., Bookman, R., Sharon, D., Gvirtzman, H., Dayan, U., Ziv, B., and Stein, M.: Late Holocene
1009 climates of the Near East deduced from Dead Sea level variations and modern regional winter rainfall, *Quat.*
1010 *Res.*, 60, 263–273, <https://doi.org/10.1016/j.yqres.2003.07.011>, 2003.

1011 Enzel, Y., Agnon, A., and Stein, M.: *New Frontiers in Dead Sea Paleoenvironmental Research*,
1012 Geological Society of America, <https://doi.org/10.1130/SPE401>, 2006.

1013 Enzel, Y., Amit, R., Dayan, U., Crouvi, O., Kahana, R., Ziv, B., and Sharon, D.: The climatic and
1014 physiographic controls of the eastern Mediterranean over the late Pleistocene climates in the southern Levant
1015 and its neighboring deserts, *Glob. Planet. Change*, 60, 165–192,
1016 <https://doi.org/10.1016/j.gloplacha.2007.02.003>, 2008.

1017 Enzel, Y., Mushkin, A., Groisman, M., Calvo, R., Eyal, H., and Lensky, N.: The modern wave-induced
1018 coastal staircase morphology along the western shores of the Dead Sea, *Geomorphology*, 408, 108237,
1019 <https://doi.org/10.1016/j.geomorph.2022.108237>, 2022.

1020 Eyal, H., Dente, E., Haviv, I., Enzel, Y., Dunne, T., and Lensky, N. G.: Fluvial incision and coarse
1021 gravel redistribution across the modern Dead Sea shelf as a result of base-level fall, *Earth Surf. Process.*
1022 *Landforms*, 44, 2170–2185, <https://doi.org/10.1002/esp.4640>, 2019.

1023 Eyal, H., Enzel, Y., Meiburg, E., Vowinckel, B., and Lensky, N. G.: How Does Coastal Gravel Get
1024 Sorted Under Stormy Longshore Transport?, *Geophys. Res. Lett.*, 48, e2021GL095082,
1025 <https://doi.org/10.1029/2021GL095082>, 2021.

1026 Eyal, H., Armon, M., Enzel, Y., and Lensky, N. G.: Synoptic- to meso-scale circulation connects
1027 fluvial and coastal gravel conveyors and directional deposition of coastal landforms in the Dead Sea basin,
1028 Mendeley Data, V1, <https://doi.org/10.17632/65bhpwfrh.1>, 2022.

1029 Fagherazzi, S.: Modeling fluvial erosion and deposition on continental shelves during sea level cycles,
1030 J. Geophys. Res., 109, F03010, <https://doi.org/10.1029/2003JF000091>, 2004.

1031 ~~FROSTICK~~Frostick, L. E. and ~~REID~~Reid, I. A. N.: Climatic versus tectonic controls of fan sequences:
1032 lessons from the Dead Sea, Israel, J. Geol. Soc. London., 146, 527–538,
1033 <https://doi.org/10.1144/gsjgs.146.3.0527>, 1989.

1034 Galloway, W. E.: Process framework for describing the morphologic and stratigraphic evolution of
1035 deltaic depositional systems, 87–98, 1975.

1036 Garfunkel, Z. and Ben-Avraham, Z.: The structure of the Dead Sea basin, Tectonophysics, 266, 155–
1037 176, [https://doi.org/10.1016/S0040-1951\(96\)00188-6](https://doi.org/10.1016/S0040-1951(96)00188-6), 1996.

1038 Gertman, I. and Hecht, A.: The Dead Sea hydrography from 1992 to 2000, J. Mar. Syst., 35, 169–181,
1039 [https://doi.org/10.1016/S0924-7963\(02\)00079-9](https://doi.org/10.1016/S0924-7963(02)00079-9), 2002.

1040 Goldreich, Y.: The spatial distribution of annual rainfall in Israel ? a review, Theor. Appl. Climatol.,
1041 50, 45–59, <https://doi.org/10.1007/BF00864902>, 1994.

1042 Goldreich, Y.: The Climate of Israel, Springer US, Boston, MA, [https://doi.org/10.1007/978-1-4615-](https://doi.org/10.1007/978-1-4615-0697-3)
1043 0697-3, 2003.

1044 Goldreich, Y., Mozes, H., and Rosenfeld, D.: Radar analysis of cloud systems and their rainfall yield in
1045 Israel, Isr. J. Earth Sci, 53, 63–76, 2004.

1046 Goodwin, I. D., Mortlock, T. R., and Browning, S.: Tropical and extratropical-origin storm wave types
1047 and their influence on the East Australian longshore sand transport system under a changing climate, J.
1048 Geophys. Res. Ocean., 121, 4833–4853, <https://doi.org/10.1002/2016JC011769>, 2016.

1049 Graf, M., Sprenger, M., Lohmann, U., Seibt, C., and Hofmann, H.: Evaluating the suitability of the
1050 SWAN/COSMO-2 model system to simulate short-crested surface waves for a narrow lake with complex
1051 bathymetry, Meteorol. Zeitschrift, 22, 257–272, <https://doi.org/10.1127/0941-2948/2013/0442>, 2013.

1052 Grosse, G., Schirrmeyer, L., Kunitsky, V. V., and Hubberten, H.: The use of CORONA images in
1053 remote sensing of periglacial geomorphology: an illustration from the NE Siberian coast, Permafr. Periglac.
1054 Process., 16, 163–172, <https://doi.org/10.1002/ppp.509>, 2005.

1055 Grottole, E., Bertoni, D., Ciavola, P., and Pozzebon, A.: Short term displacements of marked pebbles in
1056 the swash zone: Focus on particle shape and size, Mar. Geol., 367, 143–158,
1057 <https://doi.org/10.1016/j.margeo.2015.06.006>, 2015.

1058 Hamdani, I., Assouline, S., Tanny, J., Lensky, I. M., Gertman, I., Mor, Z., and Lensky, N. G.: Seasonal
1059 and diurnal evaporation from a deep hypersaline lake: The Dead Sea as a case study, J. Hydrol., 562, 155–167,
1060 <https://doi.org/10.1016/j.jhydrol.2018.04.057>, 2018.

1061 Hansford, M. R. and Plink-Björklund, P.: River discharge variability as the link between climate and
1062 fluvial fan formation, Geology, 48, 952–956, <https://doi.org/10.1130/G47471.1>, 2020.

1063 Haviv, I.: Mechanics, morphology and evolution of vertical knickpoints (waterfalls) along the bedrock
1064 channels of the Dead Sea western tectonic escarpment, The Hebrew University of Jerusalem, 2007.

1065 Hersbach, H., Bell, B., Berrisford, P., Hirahara, S., Horányi, A., Muñoz-Sabater, J., Nicolas, J., Peubey,

1066 C., Radu, R., Schepers, D., Simmons, A., Soci, C., Abdalla, S., Abellan, X., Balsamo, G., Bechtold, P., Biavati,
1067 G., Bidlot, J., Bonavita, M., Chiara, G., Dahlgren, P., Dee, D., Diamantakis, M., Dragani, R., Flemming, J.,
1068 Forbes, R., Fuentes, M., Geer, A., Haimberger, L., Healy, S., Hogan, R. J., Hólm, E., Janisková, M., Keeley, S.,
1069 Laloyaux, P., Lopez, P., Lupu, C., Radnoti, G., Rosnay, P., Rozum, I., Vamborg, F., Villaume, S., and Thépaut,
1070 J.: The ERA5 global reanalysis, *Q. J. R. Meteorol. Soc.*, 146, 1999–2049, <https://doi.org/10.1002/qj.3803>, 2020.

~~1071 Van Hijum, E. and Pilarczyk, K. W.: Gravel beaches: equilibrium profile and longshore transport of
1072 coarse material under regular and irregular wave attack, *Hydraulics laboratory*, 1982.~~

1073 Hochman, A., Mercogliano, P., Alpert, P., Saaroni, H., and Bucchignani, E.: High-resolution projection
1074 of climate change and extremity over Israel using COSMO-CLM, *Int. J. Climatol.*, 38, 5095–5106,
1075 <https://doi.org/10.1002/joc.5714>, 2018.

1076 Huntington, E.: *Palestine and its Transformation*, Houghton Mifflin, 1911.

1077 Kahana, R., Ziv, B., Enzel, Y., and Dayan, U.: Synoptic climatology of major floods in the Negev
1078 Desert, Israel, *Int. J. Climatol.*, 22, 867–882, <https://doi.org/10.1002/joc.766>, 2002.

1079 Karimpour, A. and Chen, Q.: Wind wave analysis in depth limited water using OCEANLYZ, A
1080 MATLAB toolbox, *Comput. Geosci.*, 106, 181–189, <https://doi.org/10.1016/j.cageo.2017.06.010>, 2017.

1081 Kiro, Y., Goldstein, S. L., Garcia-Veigas, J., Levy, E., Kushnir, Y., Stein, M., and Lazar, B.:
1082 Relationships between lake-level changes and water and salt budgets in the Dead Sea during extreme aridities in
1083 the Eastern Mediterranean, *Earth Planet. Sci. Lett.*, 464, 211–226, <https://doi.org/10.1016/j.epsl.2017.01.043>,
1084 2017.

1085 Kunin, P., Alpert, P., and Rostkier-Edelstein, D.: Investigation of sea-breeze/foehn in the Dead Sea
1086 valley employing high resolution WRF and observations, *Atmos. Res.*, 229, 240–254,
1087 <https://doi.org/10.1016/j.atmosres.2019.06.012>, 2019.

1088 Kushnir, Y., Dayan, U., Ziv, B., Morin, E., and Enzel, Y.: Climate of the Levant, in: *Quaternary of the*
1089 *Levant*, Cambridge University Press, 31–44, <https://doi.org/10.1017/9781316106754.004>, 2017.

1090 Lekach, J. and Enzel, Y.: Flood-duration-integrated stream power and frequency magnitude of >50-
1091 year-long sediment discharge out of a hyperarid watershed, *Earth Surf. Process. Landforms*, 46, 1348–1362,
1092 <https://doi.org/10.1002/esp.5104>, 2021.

1093 Lensky, I. M. and Dayan, U.: Continuous detection and characterization of the Sea Breeze in clear sky
1094 conditions using Meteosat Second Generation, *Atmos. Chem. Phys.*, 12, 6505–6513,
1095 <https://doi.org/10.5194/acp-12-6505-2012>, 2012.

1096 Lensky, I. M. and Dayan, U.: Satellite observations of land surface temperature patterns induced by
1097 synoptic circulation, *Int. J. Climatol.*, 35, 189–195, <https://doi.org/10.1002/joc.3971>, 2015.

1098 Lensky, N. G., Dvorkin, Y., Lyakhovskiy, V., Gertman, I., and Gavrieli, I.: Water, salt, and energy
1099 balances of the Dead Sea, *Water Resour. Res.*, 41, 1–13, <https://doi.org/10.1029/2005WR004084>, 2005.

1100 Lensky, N. G., Lensky, I. M., Peretz, A., Gertman, I., Tanny, J., and Assouline, S.: Diurnal Course of
1101 Evaporation From the Dead Sea in Summer: A Distinct Double Peak Induced by Solar Radiation and Night Sea
1102 Breeze, *Water Resour. Res.*, 54, 150–160, <https://doi.org/10.1002/2017WR021536>, 2018.

1103 Longuet-Higgins, M. S.: Longshore currents generated by obliquely incident sea waves: 1, *J. Geophys.*
1104 *Res.*, 75, 6778–6789, 1970.

1105 Manspeizer, W.: The Dead Sea Rift: Impact of climate and tectonism on Pleistocene and Holocene

1106 sedimentation, 1985.

1107 Marra, F. and Morin, E.: Autocorrelation structure of convective rainfall in semiarid-arid climate
 1108 derived from high-resolution X-Band radar estimates, *Atmos. Res.*, 200, 126–138,
 1109 <https://doi.org/10.1016/j.atmosres.2017.09.020>, 2018.

1110 Marra, F., Borga, M., and Morin, E.: A Unified Framework for Extreme Subdaily Precipitation
 1111 Frequency Analyses Based on Ordinary Events, *Geophys. Res. Lett.*, 47, e2020GL090209,
 1112 <https://doi.org/10.1029/2020GL090209>, 2020.

1113 Marra, F., Armon, M., Adam, O., Zoccatelli, D., Gazal, O., Garfinkel, C. I., Rostkier-Edelstein, D.,
 1114 Dayan, U., Enzel, Y., and Morin, E.: Toward Narrowing Uncertainty in Future Projections of Local Extreme
 1115 Precipitation, *Geophys. Res. Lett.*, 48, e2020GL091823, <https://doi.org/10.1029/2020GL091823>, 2021.

1116 Marra, F., Armon, M., and Morin, E.: Coastal and orographic effects on extreme precipitation revealed
 1117 by weather radar observations, *Hydrol. Earth Syst. Sci.*, 26, 1439–1458, [https://doi.org/10.5194/hess-26-1439-](https://doi.org/10.5194/hess-26-1439-2022)
 1118 2022, 2022.

1119 https://doi.org/https://doi.org/10.1142/9789811275135_0031_2023.
 1120 https://doi.org/https://doi.org/10.1142/9789811275135_0031_2023.
 1121 https://doi.org/https://doi.org/10.1142/9789811275135_0031_2023.
 1122 https://doi.org/https://doi.org/10.1142/9789811275135_0031_2023.

1123 Meadows, G. A., Meadows, L. A., Wood, W. L., Hubertz, J. M., and Perlin, M.: The Relationship
 1124 between Great Lakes Water Levels, Wave Energies, and Shoreline Damage, *Bull. Am. Meteorol. Soc.*, 78, 675–
 1125 682, [https://doi.org/10.1175/1520-0477\(1997\)078<0675:TRBGLW>2.0.CO;2](https://doi.org/10.1175/1520-0477(1997)078<0675:TRBGLW>2.0.CO;2), 1997.

1126 Merz, B., Blöschl, G., Vorogushyn, S., Dottori, F., Aerts, J. C. J. H., Bates, P., Bertola, M., Kemter,
 1127 M., Kreibich, H., Lall, U., and Macdonald, E.: Causes, impacts and patterns of disastrous river floods, *Nat. Rev.*
 1128 *Earth Environ.*, 2, 592–609, <https://doi.org/10.1038/s43017-021-00195-3>, 2021.

1129 Meyer-Peter, E. and Müller, R.: Formulas for bed-load transport, in: IAHSR 2nd meeting, Stockholm,
 1130 appendix 2, 1948.

1131 Molina, R., Manno, G., Lo Re, C., Anfuso, G., and Ciraolo, G.: Storm Energy Flux Characterization
 1132 along the Mediterranean Coast of Andalusia (Spain), *Water*, 11, 509, <https://doi.org/10.3390/w11030509>, 2019.

1133 Montgomery, D. R. and Buffington, J. M.: Channel-reach morphology in mountain drainage basins,
 1134 *Bull. Geol. Soc. Am.*, 109, 596–611, [https://doi.org/10.1130/0016-7606\(1997\)109<0596:CRMIMD>2.3.CO;2](https://doi.org/10.1130/0016-7606(1997)109<0596:CRMIMD>2.3.CO;2),
 1135 1997.

1136 Morin, E., Jacoby, Y., Navon, S., and Bet-Halachmi, E.: Towards flash-flood prediction in the dry
 1137 Dead Sea region utilizing radar rainfall information, *Adv. Water Resour.*, 32, 1066–1076,
 1138 <https://doi.org/10.1016/j.advwatres.2008.11.011>, 2009.

1139 ~~Ben Moshe, L., Haviv, I., Enzel, Y., Zilberman, E., and Matmon, A.: Incision of alluvial channels in
 1140 response to a continuous base-level fall: Field characterization, modeling, and validation along the Dead Sea,
 1141 *Geomorphology*, 93, 524–536, <https://doi.org/10.1016/j.geomorph.2007.03.014>, 2008.~~

1142 Mulder, T. and Syvitski, J. P. M.: Climatic and Morphologic Relationships of Rivers: Implications of
 1143 Sea-Level Fluctuations on River Loads, *J. Geol.*, 104, 509–523, <https://doi.org/10.1086/629849>, 1996.

1144 Naor, R., Potchter, O., Shafir, H., and Alpert, P.: An observational study of the summer Mediterranean
 1145 Sea breeze front penetration into the complex topography of the Jordan Rift Valley, *Theor. Appl. Climatol.*, 127,

1146 275–284, <https://doi.org/10.1007/s00704-015-1635-3>, 2017.

1147 Neev, D. and Emery, K. O.: The Dead Sea: depositional processes and environments of evaporites,
1148 1967.

1149 Neugebauer, I., Schwab, M. J., Waldmann, N. D., Tjallingii, R., Frank, U., Hadzhiivanova, E.,
1150 Naumann, R., Taha, N., Agnon, A., Enzel, Y., and Brauer, A.: Hydroclimatic variability in the Levant during the
1151 early last glacial (~117–75 ka) derived from micro-facies analyses of deep Dead Sea sediments, *Clim. Past*, 12,
1152 75–90, <https://doi.org/10.5194/cp-12-75-2016>, 2016.

1153 [Nienhuis, J. H., Ashton, A. D., and Giosan, L.: What makes a delta wave-dominated?, *Geology*, 43,
1154 511–514, <https://doi.org/10.1130/G36518.1>, 2015.](https://doi.org/10.1130/G36518.1)

1155 [Nienhuis, J. H., Ashton, A. D., and Giosan, L.: Littoral steering of deltaic channels, *Earth Planet. Sci.
1156 Lett.*, 453, 204–214, <https://doi.org/10.1016/j.epsl.2016.08.018c>, 2016.](https://doi.org/10.1016/j.epsl.2016.08.018c)

1157 Palchan, D., Neugebauer, I., Amitai, Y., Waldmann, N. D., Schwab, M. J., Dulski, P., Brauer, A.,
1158 Stein, M., Erel, Y., and Enzel, Y.: North Atlantic controlled depositional cycles in MIS 5e layered sediments
1159 from the deep Dead Sea basin, *Quat. Res.*, 87, 168–179, <https://doi.org/10.1017/qua.2016.10>, 2017.

1160 Postma, G.: An analysis of the variation in delta architecture, *Terra Nov.*, 2, 124–130,
1161 <https://doi.org/10.1111/j.1365-3121.1990.tb00052.x>, 1990.

1162 Postma, G.: Sea-level-related architectural trends in coarse-grained delta complexes, *Sediment. Geol.*,
1163 98, 3–12, [https://doi.org/10.1016/0037-0738\(95\)00024-3](https://doi.org/10.1016/0037-0738(95)00024-3), 1995.

1164 Pringle, J. and Stretch, D. D.: On a new statistical wave generator based on atmospheric circulation
1165 patterns and its applications to coastal shoreline evolution, *Comput. Geosci.*, 149, 104707,
1166 <https://doi.org/10.1016/j.cageo.2021.104707>, 2021.

1167 Pringle, J., Stretch, D. D., and Bárdossy, A.: Automated classification of the atmospheric circulation
1168 patterns that drive regional wave climates, *Nat. Hazards Earth Syst. Sci.*, 14, 2145–2155,
1169 <https://doi.org/10.5194/nhess-14-2145-2014>, 2014.

1170 Pringle, J., Stretch, D. D., and Bárdossy, A.: On linking atmospheric circulation patterns to extreme
1171 wave events for coastal vulnerability assessments, *Nat. Hazards*, 79, 45–59, [https://doi.org/10.1007/s11069-015-
1172 1825-4](https://doi.org/10.1007/s11069-015-

1172 1825-4), 2015.

1173 Reid, I., Frostick, L. E., and Layman, J. T.: The incidence and nature of bedload transport during flood
1174 flows in coarse-grained alluvial channels, *Earth Surf. Process. Landforms*, 10, 33–44,
1175 <https://doi.org/10.1002/esp.3290100107>, 1985.

1176 Rinat, Y., Marra, F., Armon, M., Metzger, A., Levi, Y., Khain, P., Vadislavsky, E., Rosensaft, M., and
1177 Morin, E.: Hydrometeorological analysis and forecasting of a 3 d flash-flood-triggering desert rainstorm, *Nat.
1178 Hazards Earth Syst. Sci.*, 21, 917–939, <https://doi.org/10.5194/nhess-21-917-2021>, 2021.

1179 Rodwell, M. J. and Hoskins, B. J.: Monsoons and the dynamics of deserts, *Q. J. R. Meteorol. Soc.*, 122,
1180 1385–1404, <https://doi.org/10.1002/qj.49712253408>, 1996.

1181 Saaroni, H., Ziv, B., Bitan, A., and Alpert, P.: Easterly Wind Storms over Israel, *Theor. Appl.
1182 Climatol.*, 59, 61–77, <https://doi.org/10.1007/s007040050013>, 1998.

1183 Saaroni, H., Halfon, N., Ziv, B., Alpert, P., and Kutiel, H.: Links between the rainfall regime in Israel
1184 and location and intensity of Cyprus lows, *Int. J. Climatol.*, 30, 1014–1025, <https://doi.org/10.1002/joc.1912>,
1185 2010.

1186 Segal, M., Mahrer, Y., and Pielke, R. A.: A study of meteorological patterns associated with a lake
1187 confined by mountains—the Dead Sea case, *Q. J. R. Meteorol. Soc.*, 109, 549–564, 1983.

1188 Sharon, D.: The spottiness of rainfall in a desert area, *J. Hydrol.*, 17, 161–175,
1189 [https://doi.org/10.1016/0022-1694\(72\)90002-9](https://doi.org/10.1016/0022-1694(72)90002-9), 1972.

1190 Sharon, D. and Kutiel, H.: The distribution of rainfall intensity in Israel, its regional and seasonal
1191 variations and its climatological evaluation, *J. Climatol.*, 6, 277–291, <https://doi.org/10.1002/joc.3370060304>,
1192 1986.

1193 Shentsis, I., Laronne, J. B., and Alpert, P.: Red Sea Trough flood events in the Negev, Israel (1964–
1194 2007), *Hydrol. Sci. J.*, 57, 42–51, <https://doi.org/10.1080/02626667.2011.636922>, 2012.

1195 Shohami, D., Dayan, U., and Morin, E.: Warming and drying of the eastern Mediterranean: Additional
1196 evidence from trend analysis, *J. Geophys. Res. Atmos.*, 116, n/a–n/a, <https://doi.org/10.1029/2011JD016004>,
1197 2011.

1198 Sirota, I., Enzel, Y., Mor, Z., Ben Moshe, L., Eyal, H., Lowenstein, T. K., and Lensky, N. G.:
1199 Sedimentology and stratigraphy of a modern halite sequence formed under Dead Sea level fall, *Sedimentology*,
1200 68, 1069–1090, <https://doi.org/10.1111/sed.12814>, 2021.

1201 Solari, S. and Alonso, R.: A New Methodology for Extreme Waves Analysis Based on Weather-
1202 Patterns Classification Methods, *Coast. Eng. Proc.*, 23, <https://doi.org/10.9753/icce.v35.waves.23>, 2017.

1203 Steirou, E., Gerlitz, L., Apel, H., and Merz, B.: Links between large-scale circulation patterns and
1204 streamflow in Central Europe: A review, *J. Hydrol.*, 549, 484–500, 2017.

1205 Syvitski, J. P. M. and Milliman, J. D.: Geology, Geography, and Humans Battle for Dominance over
1206 the Delivery of Fluvial Sediment to the Coastal Ocean, *J. Geol.*, 115, 1–19, <https://doi.org/10.1086/509246>,
1207 2007.

1208 Syvitski, J. P. M., Kettner, A. J., Overeem, I., Hutton, E. W. H., Hannon, M. T., Brakenridge, G. R.,
1209 Day, J., Vörösmarty, C., Saito, Y., Giosan, L., and Nicholls, R. J.: Sinking deltas due to human activities, *Nat.*
1210 *Geosci.*, 2, 681–686, <https://doi.org/10.1038/ngeo629>, 2009.

1211 Torfstein, A., Goldstein, S. L., Stein, M., and Enzel, Y.: Impacts of abrupt climate changes in the
1212 Levant from Last Glacial Dead Sea levels, *Quat. Sci. Rev.*, 69, 1–7,
1213 <https://doi.org/10.1016/j.quascirev.2013.02.015>, 2013.

1214 Torfstein, A., Goldstein, S. L., Kushnir, Y., Enzel, Y., Haug, G., and Stein, M.: Dead Sea drawdown
1215 and monsoonal impacts in the Levant during the last interglacial, *Earth Planet. Sci. Lett.*, 412, 235–244,
1216 <https://doi.org/10.1016/j.epsl.2014.12.013>, 2015.

1217 [Torfstein, A. and Enzel, Y.: Dead Sea lake level changes and Levant palaeoclimate, *Quat. Levant*, 115–](https://doi.org/https://doi.org/10.1017/9781316106754.013)
1218 [126, <https://doi.org/https://doi.org/10.1017/9781316106754.013>, 2017.](https://doi.org/https://doi.org/10.1017/9781316106754.013)

1219 Tsvieli, Y. and Zangvil, A.: Synoptic climatological analysis of Red Sea Trough and non-Red Sea
1220 Trough rain situations over Israel, *Adv. Geosci.*, 12, 137–143, <https://doi.org/10.5194/adgeo-12-137-2007>,
1221 2007.

1222 Tyrllis, E. and Lelieveld, J.: Climatology and Dynamics of the Summer Etesian Winds over the Eastern
1223 Mediterranean*, *J. Atmos. Sci.*, 70, 3374–3396, <https://doi.org/10.1175/JAS-D-13-035.1>, 2013.

1224 de Vries, A. J., Tyrllis, E., Edry, D., Krichak, S. O., Steil, B., and Lelieveld, J.: Extreme precipitation
1225 events in the Middle East: Dynamics of the Active Red Sea Trough, *J. Geophys. Res. Atmos.*, 118, 7087–7108,

1226 <https://doi.org/10.1002/jgrd.50569>, 2013.

1227 [Van Hijum, E. and Pilarczyk, K. W.: Gravel beaches: equilibrium profile and longshore transport of](#)

1228 [coarse material under regular and irregular wave attack, *Hydraulics laboratory*, 1982.](#)

1229 Vüllers, J., Mayr, G. J., Corsmeier, U., and Kottmeier, C.: Characteristics and evolution of diurnal

1230 foehn events in the Dead Sea valley, *Atmos. Chem. Phys.*, 18, 18169–18186, [https://doi.org/10.5194/acp-18-](https://doi.org/10.5194/acp-18-18169-2018)

1231 18169-2018, 2018.

1232 Wang, C., Zheng, S., Wang, P., and Hou, J.: Interactions between vegetation, water flow and sediment

1233 transport: A review, *J. Hydrodyn.*, 27, 24–37, [https://doi.org/10.1016/S1001-6058\(15\)60453-X](https://doi.org/10.1016/S1001-6058(15)60453-X), 2015.

1234 [WRIGHTWeisbrod, N., Yechieli, Y., Shandalov, S., and Lensky, N.: On the viscosity of natural hyper-](#)

1235 [saline solutions and its importance: The Dead Sea brines, *J. Hydrol.*, 532, 46–51.](#)

1236 <https://doi.org/https://doi.org/10.1016/j.jhydrol.2015.11.036>, 2016.

1237 [Wright, L. D.: Sediment transport and deposition at river mouths: A synthesis, *Geol. Soc. Am. Bull.*,](#)

1238 88, 857, [https://doi.org/10.1130/0016-7606\(1977\)88<857:STADAR>2.0.CO;2](https://doi.org/10.1130/0016-7606(1977)88<857:STADAR>2.0.CO;2), 1977.

1239 Zak, I.: The geology of Mt. Sedom, Hebrew University, 1967.

1240 Zappa, G., Hoskins, B. J., and Shepherd, T. G.: The dependence of wintertime Mediterranean

1241 precipitation on the atmospheric circulation response to climate change, *Environ. Res. Lett.*, 10, 104012,

1242 <https://doi.org/10.1088/1748-9326/10/10/104012>, 2015.

1243 Zittis, G., Almazroui, M., Alpert, P., Ciais, P., Cramer, W., Dahdal, Y., Fnais, M., Francis, D.,

1244 Hadjinicolaou, P., Howari, F., Jrrar, A., Kaskaoutis, D. G., Kulmala, M., Lazoglou, G., Mihalopoulos, N., Lin,

1245 X., Rudich, Y., Sciare, J., Stenchikov, G., Xoplaki, E., and Lelieveld, J.: Climate Change and Weather Extremes

1246 in the Eastern Mediterranean and Middle East, *Rev. Geophys.*, 60, e2021RG000762,

1247 <https://doi.org/10.1029/2021RG000762>, 2022.

1248 Ziv, B., Saaroni, H., and Alpert, P.: The factors governing the summer regime of the eastern

1249 Mediterranean, *Int. J. Climatol.*, 24, 1859–1871, <https://doi.org/10.1002/joc.1113>, 2004.

1250 Ziv, B., Harpaz, T., Saaroni, H., and Blender, R.: A new methodology for identifying daughter

1251 cyclogenesis: application for the Mediterranean Basin, *Int. J. Climatol.*, 35, 3847–3861,

1252 <https://doi.org/10.1002/joc.4250>, 2015.

1253 Ziv, B., Saaroni, H., Etkin, A., Harpaz, T., and Shendrik, L.: Formation of cyclones over the East

1254 Mediterranean within Red-Sea Troughs, *Int. J. Climatol.*, 42, 577–596, <https://doi.org/10.1002/joc.7261>, 2022.

1255 Zoccatelli, D., Marra, F., Armon, M., Rinat, Y., Smith, J. A., and Morin, E.: Contrasting rainfall-runoff

1256 characteristics of floods in desert and Mediterranean basins, *Hydrol. Earth Syst. Sci.*, 23, 2665–2678,

1257 <https://doi.org/10.5194/hess-23-2665-2019>, 2019.

1258

Formatted: Font: (Default) Times New Roman

Formatted: Left, Indent: First line: 1.27 cm, No widow/orphan control, Don't adjust space between Latin and Asian text, Don't adjust space between Asian text and numbers